Progressive Cl^- channel defects reveal disrupted skeletal muscle maturation in R6/2 Huntington's mice

Daniel R. Miranda,[1,2] Monica Wong,[1] Shannon H. Romer,[2] Cynthia McKee,[1] Gabriela Garza-Vasquez,[1] Alyssa C. Medina,[1] Volker Bahn,[2] Andrew D. Steele,[1] Robert J. Talmadge,[1] and Andrew A. Voss[2]

[1]Department of Biological Sciences, California State Polytechnic University, Pomona, Pomona, CA 91768
[2]Department of Biological Sciences, Wright State University, Dayton, OH 45435

Huntington's disease (HD) patients suffer from progressive and debilitating motor dysfunction. Previously, we discovered reduced skeletal muscle chloride channel (ClC-1) currents, inwardly rectifying potassium (Kir) channel currents, and membrane capacitance in R6/2 transgenic HD mice. The ClC-1 loss-of-function correlated with increased aberrant mRNA processing and decreased levels of full-length ClC-1 mRNA (*Clcn1* gene). Physiologically, the resulting muscle hyperexcitability may help explain involuntary contractions of HD. In this study, the onset and progression of these defects are investigated in R6/2 mice, ranging from 3 wk old (presymptomatic) to 9–13 wk old (late-stage disease), and compared with age-matched wild-type (WT) siblings. The R6/2 ClC-1 current density and level of aberrantly spliced *Clcn1* mRNA remain constant with age. In contrast, the ClC-1 current density increases, and the level of aberrantly spliced *Clcn1* mRNA decreases with age in WT mice. The R6/2 ClC-1 properties diverge from WT before the onset of motor symptoms, which occurs at 5 wk of age. The relative decrease in R6/2 muscle capacitance also begins in 5-wk-old mice and is independent of fiber atrophy. Kir current density is consistently lower in R6/2 compared with WT muscle. The invariable R6/2 ClC-1 properties suggest a disruption in muscle maturation, which we confirm by measuring elevated levels of neonatal myosin heavy chain (MyHC) in late-stage R6/2 skeletal muscle. Similar changes in ClC-1 and MyHC isoforms in the more slowly developing Q175 HD mice suggest an altered maturational state is relevant to adult-onset HD. Finally, we find nuclear aggregates of muscleblind-like protein 1 without predominant CAG repeat colocalization in R6/2 muscle. This is unlike myotonic dystrophy, another trinucleotide repeat disorder with similar ClC-1 defects, and suggests a novel mechanism of aberrant mRNA splicing in HD. These early and progressive skeletal muscle defects reveal much needed peripheral biomarkers of disease progression and better elucidate the mechanism underlying HD myopathy.

The Journal of General Physiology

INTRODUCTION

Huntington's disease (HD) is a fatal degenerative disorder caused by an expanded CAG repeat sequence at the 5′ end of the *Huntingtin* gene (MacDonald et al., 1993). The characteristic motor and cognitive symptoms progress in severity over the time course of the disease (Bates et al., 2002). At the early stage of HD, the motor symptoms include minor motor abnormalities such as fidgeting and restlessness. By the middle stage, patients exhibit symptoms including chorea, bradykinesia, dystonia, and muscle rigidity. By the late stage, the choreic symptoms subside and the bradykinesia, dystonia, and rigidity can become debilitating (Bates et al., 2002). Although the cognitive and psychiatric symptoms of HD are likely caused by degeneration of the striatum and cortex, the motor symptoms may be caused by cell-autonomous effects of the mutant *Huntingtin* gene in skeletal muscle.

There is a growing body of evidence showing skeletal muscle pathology in HD, including metabolic and mitochondrial defects (Lodi et al., 2000; Turner et al., 2007), molecular changes leading to atrophy (She et al., 2011; Ehrnhoefer et al., 2014), and loss of strength (Busse et al., 2008). Muscle-specific changes in HD gene expression include decreased expression of actin, myosin light chain, and troponin, which are important for muscle differentiation (Luthi-Carter et al., 2002; Strand et al., 2005). Interestingly, the onset of skeletal muscle abnormalities in HD may precede neurodegeneration and, in part, cause motor symptoms, as shown by the marathon runner who exhibited HD motor symptoms well before any neurological symptoms (Kosinski et al., 2007).

Previously, we discovered that muscle chloride channel (ClC-1) and inwardly rectifying potassium (Kir) channel currents were reduced in skeletal muscle from the transgenic R6/2 mouse model for HD near

Correspondence to Andrew A. Voss: andrew.voss@wright.edu

Abbreviations used: 9AC, anthracene-9-carboxylic acid; C_m, specific membrane capacitance; DAPI, 4′,6-diamidino-2-phenylindole; FDB, flexor digitorum brevis; FISH, fluorescent in situ hybridization; $G_{ClC\text{-}1}$, ClC-1 conductance; G_{Kir}, Kir conductance; HD, Huntington's disease; $I_{ClC\text{-}1}$, ClC-1 current; IF, immunofluorescence; I_{Kir}, Kir current; IO, interosseous; Kir, inwardly rectifying potassium; MyHC, myosin heavy chain; TA, tibialis anterior; t-tubular, transverse tubular.

The Rockefeller University Press $30.00
J. Gen. Physiol. 2017 Vol. 149 No. 1 55–74
https://doi.org/10.1085/jgp.201611603

the terminal stage of the disease (~12 wk of age) compared with age-matched WT siblings (Waters et al., 2013). These reductions correlated with decreased levels of full-length mRNA for both ClC-1 (*Clcn1*) and Kir (*Kcnj2*) ion channels as well as aberrant splicing of *Clcn1* mRNA. Additionally, the specific membrane capacitance (C_m) of R6/2 muscle fibers was reduced compared with WT. The reduced chloride currents and aberrantly spliced *Clcn1* mRNA in R6/2 fibers were similar to reported mechanisms in myotonic dystrophy, type 1, in which ClC-1 down-regulation has been linked to the sequestration of mRNA binding proteins such as muscleblind-like protein 1 (MBNL1; Mankodi et al., 2002; Lin et al., 2006). The reduced chloride and Kir currents (I_{ClC-1} and I_{Kir}) cause muscle hyperexcitability and could underlie the myotonic symptoms of HD such as dystonia, rigidity, and bradykinesia. Because our previous work was performed only on severely symptomatic R6/2 mice at the end of the disease, the onset and progression of ClC-1 and Kir defects and their relationship to disease were unknown. In this study, we determined the time course over which the following R6/2 muscle defects develop, reduced I_{ClC-1} and I_{Kir}, lower C_m, decreased full-length *Clcn1* and *Kcnj2* mRNA, and increased aberrantly spliced *Clcn1* mRNA.

MATERIALS AND METHODS

Ethical approval

All animal procedures were performed in accordance with the policies of the Animal Care and Use Committees of the California State Polytechnic University, Pomona and Wright State University.

Animal husbandry

Each breeding pair consisted of one WT female with an ovarian transplant containing the mutated *Huntingtin* gene (stock# 002810) and one WT male (B6CBAF1/J) from the Jackson Laboratory. Six breeding pairs produced a total of 41 HD (R6/2) mice and 50 WT mice. Q175 mice were provided by R. Cachope of the Cure Huntington's Disease Initiative (CHDI, New York, NY). Environmental conditions were maintained with a 12-h light/dark cycle and constant temperature (21–23°C) and humidity (55 ± 10%). The cages contained sanichip bedding (product 7090; Envigo) and environmental enrichment (mouse house and cotton nestlet). Mice were supplied with dry chow (irradiated rodent diet; Harlan Teklad 2018) and water ad libitum. At 10 wk of age, the R6/2 mice were supplied with supplemental food and water in the form of Hydrogel and mash (dry chow moistened until paste-like in consistency) in a Petri dish placed on the cage floor. Cages were changed every 1 wk or as needed.

Mouse monitoring and behavioral assessment

The physical condition of the mice was assessed weekly in mice <10 wk of age and daily in mice ≥10 wk of age. Assessment categories were physical condition, approximate respiratory rate, activity level, consumption of water and food, body mass loss, and hind limb clasping. Each category was rated on a scale of 0–3, with 0 marking normal condition and 3 representing extremely poor condition. Mice were euthanized (and used for experimentation) if the sum of the first five category scores was greater than or equal to 6 or if the score of any individual category was equal to 3, which in all cases occurred during late stage.

Video-based home cage activity data were analyzed using HomeCageScan 3.0; behavioral definitions were as described previously (Steele et al., 2007). Mice were single housed and habituated to standard microisolater cages for 24 h and then video recorded for an additional 24 h. The percentage of time spent hanging, jumping, rearing, or walking was calculated by dividing the sum (in seconds) of each of these behaviors by the sum of all scored behaviors (only one behavior can be assigned at any given time).

Electrophysiology

Mice were euthanized by inhalation of a 2-g/liter dose of isoflurane for at least 1 min, followed by cervical dislocation. Flexor digitorum brevis (FDB) and interosseous (IO) muscle fibers were removed, pinned to Sylgard-bottomed Petri dishes, and enzymatically dissociated at 35–36°C under mild agitation for ~1 h using 1,000 U/ml of collagenase type IV (Worthington Biochemical). Collagenase was dissolved in the extracellular solution (below). Dissociation was completed using mild trituration in extracellular solution with no collagenase. The fibers were allowed to recover at 21–23°C for 1 h before electrical measurements were recorded.

Fibers were visualized in a BX51WI or IX71 microscope (Olympus), and images were acquired with a CCD camera (ST-7XMEI-C1 or STF8300M; Santa Barbara Instruments). The BX51WI microscope was equipped with 10× (UMPLFLN10XW) and 40× (LUM PLFLN40XW) objectives; 20× images were obtained with a 2× intermediate magnification changer. The IX71 microscope was equipped with 10× (UPlanFLN) and 20× (UPlanFLN) objectives. ImageJ (National Institutes of Health) and SigmaPlot13 (Systat) were used to determine the fiber surface area assuming a cylindrical shape. The mean fiber length (l) was obtained from at least two measurements of length near each edge and one measurement from the middle of the fiber. Because a two-dimensional image of a cylinder is a rectangle, r was obtained from the equation, r = (two-dimensional surface area)/(2l). This provided a more reliable method of estimating r than measuring the diameter of

the fiber at numerous points along its length. The equation for a cylinder was used to estimate the three-dimensional fiber surface area (surface area = $2\pi rl + 2\pi r^2$).

Electrical properties were measured under standard current and voltage-clamp conditions at 21–23°C using two borosilicate intracellular microelectrodes with a 1.5-mm outside diameter and 0.86-mm inside diameter (Sutter Instrument), an Axoclamp 900A amplifier, a Digidata 1550 digitizer, and pCLAMP 10 data acquisition and analysis software (Molecular Devices). The Axoclamp 900A was equipped with a virtual-ground headstage (VG-9Ax100). Reference electrodes were placed in separate cups containing 3 M KCl and connected to the extracellular fluid via agar bridges. Electrodes were impaled ∼50 µm apart from each other, or roughly within the diameter of the fiber. The voltage-sensing electrode was connected with an Axoclamp HSx1 headstage. The current-passing electrode was connected with an Axoclamp HSx10 headstage that was modified to have a 2-MΩ output resistor (HSx5). Both the current-passing and voltage-sensing electrodes were filled with the same internal solution (below). The electrode resistance was between 4 and 16 MΩ. After impalement, 20 min was given for equilibration of the electrode solution with the sarcoplasm before data acquisition. A high concentration of EGTA was used in the internal solutions to prevent contractions. Data were acquired at 100 kHz. Current and voltage records were low-pass filtered with the internal Axoclamp 900A filters at 2 kHz. The voltage-clamp command signal was low-pass filtered with an external Warner LFP-8 at 2 kHz.

Fiber capacitance and leak conductance were obtained under voltage-clamp conditions in the same fibers used to determine the chloride and potassium currents, as described previously (Waters et al., 2013). To minimize errors caused by voltage-activated channels, measurements were made at the end of the experiments after the major Na^+, K^+, Ca^{2+}, and Cl^- channels were blocked with tetrodotoxin, Cs^+ substitution, nifedipine, and anthracene-9-carboxylic acid (9AC), respectively. Fiber capacitance was measured by integrating the capacitive transients from an equal number of positive and negative 20-ms voltage steps from the holding potential. The leak conductance was obtained from the same voltage jumps by determining the slope of the steady-state current-voltage relationship. Leak conductances were normalized to the fiber capacitance.

For data analysis, healthy fibers were chosen based on equilibrium potential and leak conductance. Fibers with a measured reversal potential of ±5 mV of the chloride equilibrium potential or ±10 mV of the potassium equilibrium potential were chosen for chloride and potassium currents, respectively. Only fibers normalized to leak conductance within a standard deviation of the mean value were included for analysis.

Intracellular and extracellular buffers for electrophysiology

Intracellular chloride solution (mM). 17 aspartate, 30 HCl, 30 EGTA, 15 $CaCl_2$, 5 $MgCl_2$, 5 ATP di-Na, 5 phosphocreatine di-Na, 5 glutathione, and 20 MOPS, pH 7.2 with CsOH.

Intracellular potassium solution (mM). 75 aspartate, 15 $Ca(OH)_2$, 30 EGTA, 5 $MgCl_2$, 5 ATP disodium, 5 phosphocreatine di-Na, 5 glutathione, and 20 MOPS, pH 7.2 with KOH.

Extracellular solution (mM). 135 NaCl, 4 KCl, 5 $CaCl_2$, 2 $MgCl_2$, 5 glucose, 1 NaH_2PO_4, and 10 MOPS, pH 7.4 with NaOH.

Extracellular chloride solution (mM). 140 HCl, 2 CsOH, 2 $CaCl_2$, 1 $MgCl_2$, 5 glucose, 1 NaH_2PO_4, 10 MOPS, 0.0002 tetrodotoxin, and 0.02 nifedipine, pH 7.4 with TEA hydroxide. 0.4 9AC was added for ClC-1 conductance ($G_{ClC\text{-}1}$) blocking solution.

Extracellular potassium solution (mM). 130 KCl, 12.5 NaCl, 5 $CaCl_2$, 2 $MgCl_2$, 5 glucose, 1 NaH_2PO_4, 10 MOPS, 0.0002 tetrodotoxin, 0.02 nifedipine, and 0.4 9AC, pH 7.4 with NaOH. 5 $BaCl_2$ was added for Kir conductance (G_{Kir}) blocking solution.

Chemicals

Chemicals were purchased from Thermo Fisher Scientific; exceptions include $CaCl_2$ and $MgCl_2$ stock solutions (TekNova), CsOH and TEA hydroxide (Alfa Aesar), ATP di-Na and nifedipine (Sigma-Aldrich), $BaCl_2$ (Matheson, Coleman and Bell), tetrodotoxin (Abcam), and 9AC (Tocris Bioscience).

RNA analysis

Tibialis anterior (TA) muscles were removed from euthanized R6/2 mice, frozen in liquid nitrogen, and stored at −80°C. Total RNA was isolated from muscle samples using the RNeasy Fibrous Tissue Mini kit (QIA GEN). TA muscles were removed from mice at the same time as FDB and IO. TA samples were chosen based on age and were not dependent on electrophysiological experiments. 1 µg RNA was reverse transcribed to synthesize cDNA. For analysis of alternatively spliced gene products (inclusion of exon 7a) of *Clcn1*, PCR was performed for 30 cycles, annealing at 52°C using Platinum *Taq* DNA polymerase (Invitrogen) protocol. Forward 5′-GGAATACCTCACACTCAAGGCC-3′ and reverse 5′-CACGGAACACAAAGGCACTGAATGT-3′ primers were used (Integrated DNA Technologies). PCR products were separated on 2% agarose gels, and the amplicons representing normal and aberrantly spliced mRNA products were quantified using a FluorChem SP (Alpha Innotech). For analysis of alterna-

tively spliced variants at exons 5–8, PCR was performed for 25 cycles, annealing at 51°C using the Platinum Taq DNA Polymerase (Invitrogen) protocol. Forward 5′-GCCTTTGTAGCCAAGGTGG-3′ and reverse 5′-GAA TGTGGCTGCAAAGAATCC-3′ primers were used (Integrated DNA Technologies). PCR products were separated through a 1.5% agarose gel and quantified as stated above. To quantify full-length total *Clcn1* and *Kcnj2* mRNA levels, real-time quantitative RT-PCR was performed with an MJ Research DNA engine Opticon 2. *Clcn1* was quantified using primers that spanned either exons 10–14 or exons 16–19 as previously described (Waters et al., 2013). *Kcnj2* was quantified using a TaqMan assay (Mm00434616.m1; Applied Biosystems). *Clcn1* and *Kcnj2* were normalized to β2-microglobulin (TaqMan assay Mm00437762.m1; Applied Biosystems) and analyzed using the ΔΔCT method (Livak and Schmittgen, 2001).

Myosin heavy chain (MyHC) isoform mRNAs were quantified similar to full-length *Clcn1* and *Kcnj2* mRNAs using the real-time PCR procedures and the ΔΔCT method. Expression levels were again normalized to β2-microglobulin. TaqMan assays (Applied Biosystems) Mm01332489.m1, Mm01332564.m1, Mm01332463.m1, Mm01332518.m1, Mm01319006.g1, and Mm01329494.m1 were used to quantify *myh1* (MyHC-2x), *myh2* (MyHC-2a), *myh3* (MyHC-embryonic), *myh4* (MyHC-2b), *myh7* (MyHC-1), and *myh8* (MyHC-neonatal), respectively, as described in Talmadge et al. (2014).

Clcn1 and *Kcnj2* pre-mRNA were assessed as markers for gene transcription (see for example, Huey et al. [2003] and Ponzio et al. [2007]). A semi-quantitative one-step RT-PCR protocol (One-Step with Q reagent; QIAGEN) was used to quantify pre-mRNA levels in the TA of WT and R6/2 (HD) mice. Total RNA was obtained from TA muscles of WT and HD mice ($n = 6$ per group) using the TRIzol technique (Chomczynski and Sacchi, 1987) followed by a DNase treatment (DNA-Free; Ambion) to remove genomic DNA. cDNA was synthesized from 1 µg RNA using primers designed to reverse transcribe and subsequently amplify only the specific pre-mRNA of interest (across an intron–exon boundary). Because the primers amplify a product that crosses an intron–exon boundary, *Clcn1* and *Kcnj2* mRNA would not generate reaction products. For *Clcn1*, the forward primer was located in intron 1 and the reverse primer in the following exon. For *Kcnj2*, the forward primer was located in exon 1 and the reverse primer in the following intron. For the RT-PCR step, the optimal annealing temperatures were determined using the gradient function on an MJ Research DNA Engine (56°C for Clcn1 and 60°C for Kcnj2). PCR was performed using the following temperature steps: HotStarTaq PCR activation for 15 min at 95°C and then 32 cycles of 1-min denaturing (94°C), 1-min annealing (see above), and 1-min extension (72°C), followed by final extension for 10 min (72°C), which resulted in 433-bp and 237-bp PCR products for *Clcn1* and *Kcnj2*, respectively. Because contaminating genomic DNA would also generate a similar-sized PCR product and interfere with quantification of the pre-mRNAs, PCR reactions using an equal amount of non–reverse transcribed RNA were performed. In this case, the one-step reactions were run as normal, but the RNA was added immediately after the RT step (50°C for 30 min). These reactions did not produce reaction products, demonstrating an absence of contaminating genomic DNA. PCR products were quantified on ethidium bromide–stained 1.8% agarose Tris-Borate-EDTA gels. For normalization purposes, one-step RT-PCR was performed on each sample using primers for 18S ribosomal RNA (Ambion). *Clcn1* and *Kcnj2* band intensities were normalized to 18S RNA band intensities.

Protein analysis

Western blotting for the quantification of muscleblind-like (MBNL) proteins were as follows. In brief, TA muscles from late-stage R6/2 and age-matched WT mice ($n = 5$ per group) were homogenized in 9 vol of radioimmunoprecipitation assay buffer with a protease inhibitor cocktail added (cOmplete, Mini EDTA-free protease inhibitor cocktail; Sigma-Aldrich). The homogenates were centrifuged at 1,000 *g* for 10 min at 4°C, and the supernatants were saved at −80°C for analysis. The protein contents of the TA supernatants were quantified according to Bradford (1976). Supernatant proteins (50 µg per sample) diluted in Laemmli sample buffer were then separated on sodium dodecyl sulfate–polyacrylamide gels (10% T). The proteins were then transferred to polyvinylidene difluoride (PVDF) membranes using a semi-dry blotting procedure. The PVDF membranes were then blocked in Tris-buffered saline containing 0.05% Tween 20 (TTBS) and 4% nonfat dry milk for 1 h. After blocking, the membranes were incubated for 18 h at 4°C in primary antibodies, MB1a(4A8) for MBNL1 (Holt et al., 2009), MB2a(3b4) for MBNL-2 (Holt et al., 2009), or an antibody against β-actin (Cell Signaling Technology). The MBNL primary antibodies were diluted 1:100 and the β-actin antibody 1:500 in blocking solution. MBNL1 and MBNL1 antibodies were developed by G.E. Morris (Centre for Inherited Neuromuscular Disease, RJAH Orthopaedic Hospital, Oswestry, England, UK). The membranes were washed in TTBS (3× 10 min) and incubated with HRP-conjugated secondary antibodies for 1 h at room temperature. After a second wash in TTBS (3× 10 min), the membranes were incubated in SuperSignal West Pico chemiluminescent substrate (Thermo Fisher Scientific) for 5 min. Chemiluminescent images and band quantification were performed using a FluorChem image analysis sys-

tem (Alpha Innotech). All Western blot images are shown as reverse images, and MBNL quantitative data are normalized to β-actin. MyHC isoforms were quantified as described in Talmadge and Roy (1993).

Fluorescent in situ hybridization (FISH) and immunofluorescence (IF)

The detection of CAG transcripts in three R6/2 and three WT mice was performed with FISH using the TYE563-labeled DNA/LNA probes 5′(CTG)$_6$-CA with modified LNA at positions 5, 8, 13, 16, and 19 (Exiqon; de Mezer et al., 2011; Mykowska et al., 2011). Frozen sections (18 µm) of whole FDB muscles were washed in PBS and fixed in modified Carnoy's (2% formalin, 25% acetic acid, and 73% ethanol) at 4°C for 30 min. After fixation, tissue was incubated in 30% formamide with 2× SSC buffer for 30 min at room temperature. Tissue was incubated with FISH probe (2 ng/µl) in hybridization buffer (30% formamide, 2× SSC, 10% dextran sulfate, 2 mM vanadyl nucleoside, and 0.02% BSA) first at 75°C for 5 min to denature the target RNA and probe and then overnight at 37°C in hybridization chamber while light protected. After hybridization, tissue was washed three times for 5 min in 30% formamide with 2× SSC buffer and then three times for 5 min in 30% formamide with 1× SSC Buffer for 15 min at room temperature.

To detect MBNL1, IF was performed using rabbit anti-MBNL1 primary antibody (1:2K, A2764; a gift from C. Thornton, University of Rochester Medical Center, Rochester, NY). After FISH, tissue was washed in PBS with 0.3% Triton X-100 (TX) for 15 min, blocked for 1 h with 10% normal horse serum (Vector Laboratories), and then incubated in primary antibody at 4°C overnight. After a wash in PBS with 0.3% TX for 15 min, immunoreactivity was detected with anti–rabbit secondary antibody conjugated to Alexa Fluor 488 (1:200; Jackson ImmunoResearch Laboratories, Inc.) for 1 h at room temperature. Tissue was washed in PBS with 0.3% TX for 15 min and then PBS for 10 min, mounted in VECTASHIELD medium with 4′,6-diamidino-2-phenylindole (DAPI; Vector Laboratories) for imaging. To confirm our observations were specific to skeletal muscle nuclei, in two R6/2 and WT mice, the FISH and IF methods were also performed in dissociated muscle preparations.

Confocal imaging and figure composition

Micrographs of fluorescently labeled FDB skeletal muscles were obtained on a FluoView 1000 (Olympus) confocal microscope with a 60× oil immersion objective (NA 1.35) at 0.2-µm z-steps for both R6/2 and WT mice. Microscope images were prepared by adjusting contrast and brightness and sharpened using a "high gauss" filter in Image Pro Plus Software (Media Cybernetics) equally in R6/2 and WT images. The information content of the images was preserved. Figures were composed using CorelDraw (v. 12.0).

Curve fitting

We assessed the relative open probability of ClC-1 using a Boltzmann equation of the form

$$\frac{I_{\text{ClC-1}}(V_\text{m})}{I_{\text{ClC-1}}max} = \frac{1}{1 + e^{-\left(\frac{V_\text{m} - V_{0.5}}{k}\right)}},$$

where $I_{\text{ClC-1}}(V_\text{m})$ is the ClC-1 current at the membrane voltage (V_m), $I_{\text{ClC-1}}max$ is the maximum $I_{\text{ClC-1}}$, $V_{0.5}$ is the midpoint of $I_{\text{ClC-1}}$ activation, and k is the voltage change required for an e-fold change in current. Linear fits were used to determine conductance values.

Statistics

A two-tailed t test was used to compare means of two independent samples that were found normal by the Shapiro-Wilk test and had equal variances based on a folded F variance ratio test. We used the Mann-Whitney rank sum test for nonnormal and/or heteroscedastic samples. Repeated measures one-way ANOVA was used to compare means of mouse weights within the same category (i.e., R6/2 or WT). For full datasets plotted as a function of age, we hypothesized that the skeletal muscle properties change in R6/2 and WT mice during maturation (3–12 wk of age) and that those changes differ between R6/2 and WT mice. Electrical characteristics of conductances (mS/cm^2 and mS/µF) and C_m (µF/cm^2) were measured on one to nine muscle fibers per mouse. The mRNA processing data were measured from one muscle sample per mouse. The number of fibers or muscle samples used in each experiment is included in relevant sections of the Results. We used linear mixed models for testing the above hypotheses and included individuals as a random variable when multiple measures were taken per individual to avoid pseudo-replication. We fit the models by maximum likelihood and tested the above hypotheses with F-tests using the Satterthwaite method for estimating denominator degrees of freedom. We included age as a continuous variable and genotype as a categorical variable (R6/2 vs. WT), as well as an interaction between the two to test the hypothesis that muscle development differs over time between WT and disease mice. The overall significance of age tested our first hypothesis that muscle characteristics change over time. We inspected model residuals visually for deviation from assumptions of normality, homoscedasticity, and patterns that would suggest a curvilinear relationship, rather than a straight line. Means were compared in SigmaPlot except for the behavior data, which was completed with Prism. All other statistical analyses were conducted in the statistical programming environment R (R Core Team 2013). Null hypotheses in all statistical tests were rejected at $\alpha \leq 0.05$.

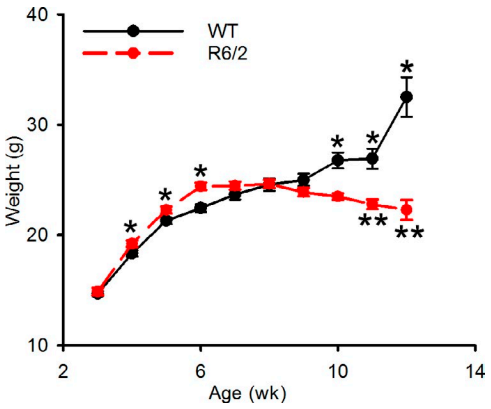

Figure 1. **Age dependence of weight.** Mean WT and R6/2 mouse weights plotted as a function of age in weeks. The *n* values represent the number of weights recorded from each mouse at different ages within the given age range. Student's *t* test indicted a significant difference (*) between WT and R6/2 mice at 4 (n_{WT} = 102, $n_{R6/2}$ = 98, P = 0.029), 5 (n_{WT} = 97, $n_{R6/2}$ = 89, P = 0.049), 6 (n_{WT} = 87, $n_{R6/2}$ = 71, P ≤ 0.001), 10 (n_{WT} = 37, $n_{R6/2}$ = 23, P = 0.002), 11 (n_{WT} = 27, $n_{R6/2}$ = 16, P = 0.002), and 12 (n_{WT} = 11, $n_{R6/2}$ = 5, P = 0.002) wk of age. The number of weight measurements decreased with age because mice used for experiments were removed from the cohort. Repeated one-way ANOVA measurements were used to assess the plateau in R6/2 weight. There was no significant difference between age groups 6–10 for R6/2 mice (P = 0.378). However, there was a significant difference (**) in R6/2 age groups between 6–11 wk (P = 0.049) and 6–12 wk (P = 0.032). Data are presented as mean and errors as SEM.

Slope values are presented ± standard errors, and mean values are presented ± SEM.

Online supplemental material

The supplemental material includes a behavioral analysis (Fig. S1), the diameters of all the fibers used for electrophysiology plotted as a function of age (Fig. S2), and the age dependence of $G_{ClC\text{-}1}$ and G_{Kir} normalized to surface area (Fig. S3).

RESULTS

Body weight and behavior

Mean mouse body weights were grouped per week of age from a total of 41 R6/2 mice and 50 age-matched WT littermates (Fig. 1). As expected, the WT mice continuously gained weight from 3–12 wk of age. From 4–6 wk of age, the R6/2 mice weighed slightly but significantly more than WT mice. However, from 6–10 wk, the R6/2 mice did not gain or lose weight. It was not until 10 wk of age that the R6/2 mice began to lose weight. From 10–12 wk, the weight of the R6/2 mice became significantly lower than WT. This reduction is consistent with previous studies (Carter et al., 1999; Ribchester et al., 2004; She et al., 2011). The R6/2 weight loss was an indicator of progression into the late stages of disease.

To confirm that motor symptoms developed in our R6/2 colony, automated behavior analysis was performed on mice in their home cage environment. R6/2 mice exhibited a significant decrease (P = 0.019) in hanging compared with WT mice at the late stage of the disease (Fig. S1), roughly corresponding to the time of weight loss in the R6/2 mice. Our previous, more detailed, study of behavior showed that the motor defects appeared in R6/2 mice as young as 7 wk of age (Steele et al., 2007), in line with several other studies (Carter et al., 1999; Ribchester et al., 2004; She et al., 2011) and near the time at which the R6/2 weight began to plateau.

Muscle chloride channels

To determine any age-dependent functional defects in the muscle chloride channel (ClC-1), $I_{ClC\text{-}1}$ values were measured from dissociated FDB or IO muscle fibers from R6/2 and WT mice using two-electrode voltage-clamp. All $I_{ClC\text{-}1}$ were normalized to membrane capacitance to obtain $I_{ClC\text{-}1}$ density (μA/μF). Fig. 2 shows the voltage- and time-dependent properties of $I_{ClC\text{-}1}$ values between age-matched WT (left) and late-stage R6/2 (right) muscle fibers obtained from a three-pulse protocol (Fig. 2 A). Late-stage R6/2 mice had a 44% reduction (P = 0.003) in peak $I_{ClC\text{-}1}$ density (−125.63 ± 12.37 μA/μF) at −140 mV compared with WT animals (−220.99 ± 33.93 μA/μF; Fig. 2 D).

$I_{ClC\text{-}1}$ was isolated by blocking Na^+, K^+, and Ca^{2+} channels with tetrodotoxin, Cs^+/TEA, and nifedipine, respectively. High intracellular chloride (70 mM) was used to maximize inward chloride currents. From a holding potential of −20 mV, the chloride equilibrium potential, ClC-1 was fully activated by applying a 150-ms conditioning pulse to 60 mV (Fig. 2 A, P1). Subsequently, the voltage dependence of the peak $I_{ClC\text{-}1}$ through the open channels was determined by applying a series of 200-ms voltage steps from −140 mV to 120 mV in increments of 20 mV (Fig. 2 A, P2). After the channels deactivated, the voltage was stepped to −100 mV for 50 ms (Fig. 2 A, P3) to determine the relative open probability. The total currents recorded in this protocol include $I_{ClC\text{-}1}$ plus the leak and capacitive currents (Fig. 2 B). To obtain specific $I_{ClC\text{-}1}$, the voltage protocol was repeated in the presence 0.4 mM 9AC, a chloride channel blocker (Fig. 2 C). The currents recorded during exposure to 9AC included only the leak and capacitive currents. Specific $I_{ClC\text{-}1}$ records were generated by subtracting the currents recorded in the presence of 9AC from the total currents recorded before 9AC (Fig. 2 D). The current-voltage (IV) relationship of the peak specific $I_{ClC\text{-}1}$ records during P2 for WT and R6/2 fibers is shown in Fig. 2 E. There was a significant reduction in R6/2 peak $I_{ClC\text{-}1}$ density compared with WT at all voltages except −20 mV, the reversal potential for Cl^-.

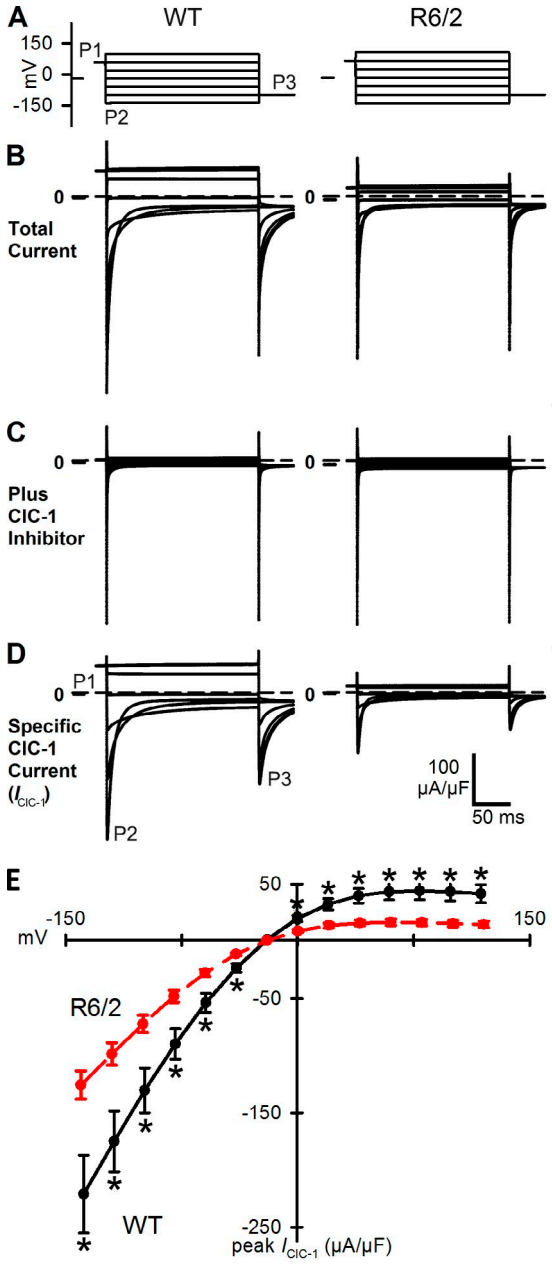

Figure 2. **Chloride current density.** Mean chloride currents from late-stage (67–93 d) WT (n = 7 fibers; 2 mice) and R6/2 (n = 18 fibers; 5 mice) muscle. (A–D) Voltage-clamp traces for WT (left) and R6/2 (right) fibers. Scale bars are shown in the bottom right. For clarity, only every other voltage and current trace is shown. (A) Voltage protocol. (B–D) Current records normalized to fiber capacitance (μF). (B) Total currents were composed of the chloride current (I_{ClC-1}) plus leak and capacitive currents. (C) Leak and capacitive currents were measured by blocking chloride channels with 400 μM 9AC. (D) Specific I_{ClC-1} records were obtained by subtracting the leak and capacitive currents (C) from the total currents (B). (E) IV relationship of the I_{ClC-1} (mean ± SEM) from P2. A significantly lower current (*) was observed from R6/2 mice compared with WT at −140 mV (P = 0.003), −120 mV (P = 0.003), −100 mV (P = 0.002), −80 mV (P = 0.002), −60 mV (P = 0.001), −40 mV (P < 0.001), 0 mV (P < 0.001), 20 mV (P < 0.001), 40 mV (P < 0.001), 60 mV (P < 0.001), 80 mV (P < 0.001), 100 mV (P < 0.001), and 120 mV (P < 0.001), but not at −20 mV (P = 0.223).

Adequate voltage control of skeletal muscle, particularly in the transverse tubular (t-tubular) system, can be difficult to obtain. Voltage-clamp errors caused by space-clamp problems will result in abrupt changes in IV profiles and poorly resolved reversal potentials (Bezanilla et al., 1982). Supporting adequate voltage control, our I_{ClC-1} values had a smooth voltage dependence and reversal potential near the predicted value of −20 mV, based on the concentrations in our intracellular (electrode) and extracellular solutions.

The specific G_{ClC-1} of the fibers in mS/μF was the slope of the IV relationship from −140 to −100 mV. To more accurately examine ClC-1 function during disease progression, the G_{ClC-1} of individual WT (n = 79 fibers; 31 mice) and R6/2 (n = 77 fibers; 23 mice) skeletal muscle fibers was plotted as a function of age (Fig. 3 A). For consistency with our previous work, Fig. 3 (A and B) also includes five fibers from four R6/2 mice and nine fibers from three WT mice from our initial characterization of ClC-1 function in HD (Waters et al., 2013). The data were analyzed with a mixed linear model. The difference in slopes between R6/2 and WT G_{ClC-1} (P = 0.019) occurred because WT G_{ClC-1} significantly increased with age (P = 0.045), whereas the R6/2 G_{ClC-1} did not change with age (P = 0.174). We estimated the age at which the R6/2 G_{ClC-1} diverged from WT mice using 95% confidence intervals (Fig. 3 B). G_{ClC-1} values in Fig. 3 B are shown as means per mouse. This is not equivalent to the inclusion of individuals as a random variable in the mixed models but is the closest possible graphical representation. Based on the intersection of the confidence intervals, the divergence between WT and R6/2 G_{ClC-1} began at ∼35 d.

By determining the relative open probability of ClC-1, we previously observed no voltage-dependent changes in ClC-1 function from late-stage R6/2 fibers compared with WT mice (Waters et al., 2013). Here, the age dependence of ClC-1 relative open probability was analyzed from the same fibers as shown in Fig. 3 (A and B). There was no difference in the voltage of half-maximal activation ($V_{0.5}$) between WT (−36.13 ± 1.44 mV) and R6/2 (−34.14 ± 1.40 mV) fibers (P = 0.32; based on n of fibers). Based on the mixed linear model, there was no change in the $V_{0.5}$ of WT (P = 0.073) or R6/2 (P = 0.653) over time, and there was no difference between the $V_{0.5}$ of WT and R6/2 over time (P = 0.659). Although not significant, the WT $V_{0.5}$ tended to slightly decrease with age (−0.17 ± 0.09 mV/day; P = 0.073). Similarly, there were no differences in the slope factor for the Boltzmann curve (k) between WT (22.59 ± 0.32) and R6/2 (22.31 ± 0.37) fibers (P = 0.57; based on n of fibers). Moreover, there was no age-dependent change in k values for WT (P = 0.495) and R6/2 (P = 0.653) fibers or a change between the WT and R6/2 k values over time (P = 0.424). This supports the normal functioning of ClC-1 over the time course of study.

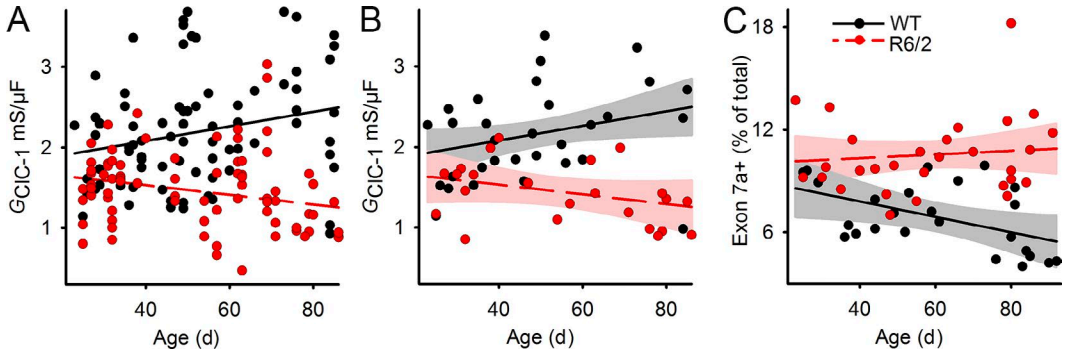

Figure 3. **Age dependence of peak chloride conductance (G_{ClC-1}) and *Clcn1* exon 7a inclusion.** (A) G_{ClC-1} of individual muscle fibers as a function of time. Linear regression lines are shown as solid black lines for WT and broken red lines for R6/2 fibers. There was a significant difference between WT and R6/2 slopes (P = 0.019), a significant increase in WT G_{ClC-1} over time (P = 0.045), and no significant change in R6/2 G_{ClC-1} over time (P = 0.174). (B) Mean G_{ClC-1} per mouse with 95% confidence intervals for WT (black) and R6/2 (red) data points. The slope of the R6/2 regression line was −0.006 ± 0.004 G_{ClC-1}/day, and the slope of the WT regression line was 0.009 ± 0.004 G_{ClC-1}/day. (C) Age dependence of aberrantly spliced *Clcn1* mRNA (with exon 7a) per mouse with 95% confidence intervals for WT (black) and R6/2 (red) data points. There was no significant change in R6/2 exon 7a+ overtime (P = 0.553), a significant decrease in WT exon 7a+ over time (P = 0.026), and a significant difference between R6/2 and WT slopes (P = 0.041). Note, two R6/2 Exon 7a+ data points overlap (32 d, 13.3%). The slope of the R6/2 regression line was 0.010 ± 0.017% exon 7a+/day and the slope of the WT regression line was −0.045 ± 0.019% exon 7a+/day.

Chloride channel mRNA

In separate experiments, the level of aberrantly spliced *Clcn1* mRNA containing exon 7a over the progression of the disease was measured from WT (n = 25 mice) and R6/2 (n = 30 mice) TA muscle (Fig. 3 C). The level of *Clcn1* mRNA with exon 7a in R6/2 skeletal muscle did not change over time (P = 0.553). In contrast, the level of *Clcn1* mRNA with exon 7a in WT muscle decreased with time (P = 0.026). Because of the different progressions, the level of exon 7a inclusion in R6/2 muscle differed from WT over time (P = 0.041). The confidence intervals of the linear regressions indicate that the level of exon 7a *Clcn1* mRNA in R6/2 skeletal muscle began to differ from WT mice at ∼35 d of age, analogous to the divergence in G_{ClC-1}.

Two additional aberrant splice variants of *Clcn1* mRNA were examined by assessing the expression of sequences between exons 5 and 8. One variant includes an exon between exons 7 and 8, called exon 8a (Mankodi et al., 2002). The other isoform includes an extension of exon 6. There was a significant (P < 0.001) increase in the combined aberrantly spliced *Clcn1* mRNA transcripts within exons 5–8 from late-stage R6/2 mice relative to WT mice (Fig. 4 A). These findings support an increase in multiple alternatively spliced *Clcn1* mRNA isoforms during disease progression.

There was a significant reduction in total full-length *Clcn1* mRNA as measured by using primers spanning exons 10–14 (Fig. 4 B, P = 0.015) and 16–19 (Fig. 4 C, P < 0.001) at the late stage of the disease. Although the levels of full-length *Clcn1* mRNA were not statistically reduced in younger muscle, the data trended toward a progressive decrease over time in experiments with both primers. This trend is in line with the age-dependent reduction in G_{ClC-1}, suggesting that aberrant splicing of *Clcn1* mRNA causes a reduction in full-length *Clcn1* mRNA and subsequently reduces the levels of functional ClC-1 proteins. To further examine the decrease in full-length *Clcn1* mRNA, pre-mRNA was measured in WT and R6/2 muscle. There was no significant change in *Clcn1* pre-mRNA in WT compared with R6/2 muscle (Fig. 4 D), suggesting that the reduction of full-length *Clcn1* mRNA was caused by a posttranscriptional defect such as aberrant mRNA splicing.

Kir channels

The age dependence of Kir channel currents (I_{Kir}) in dissociated FDB and IO muscle fibers from R6/2 and WT mice were measured using two-electrode voltage-clamp. All I_{Kir} were normalized to membrane capacitance to obtain I_{Kir} density (µA/µF). Kir channels open at potentials negative to the potassium equilibrium potential (E_K) and generate inward currents; at potentials positive to E_K, Kir channels are mostly closed (Standen and Stanfield, 1980). The subtraction approach we used was analogous to that described above for I_{ClC-1} values. The major Na^+, Cl^-, and Ca^{2+} channels were blocked with tetrodotoxin, 9AC, and nifedipine, respectively. I_{Kir} was obtained by taking the difference between the currents recorded before and during exposure to the Kir channel blocker, Ba^{2+} (5 mM).

Large inward currents were generated by using high extracellular potassium (130 mM). The predicted E_K of −10 mV was calculated using an intracellular K^+ concentration of 190 mM (electrode solution). From a holding potential of 0 mV, 700-ms pulses ranging from −60 to 20 mV were applied in 10-mV increments (Fig. 5 A). Peak I_{Kir} from late-stage R6/2 fibers were reduced compared

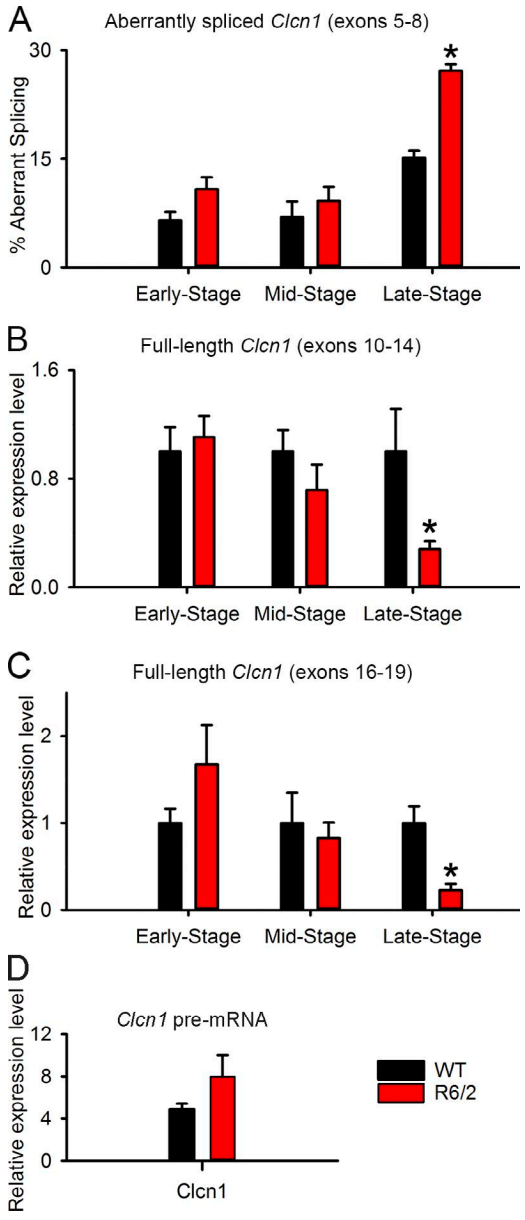

Figure 4. ***Clcn1* mRNA analysis.** Data pooled into three age groups: early (23–46 d), mid (47–66 d), and late (67–93 d) stage. (A) Relative percentage of aberrantly spliced *Clcn1* mRNA between exons 5 and 8. There was no significant difference between WT and R6/2 mice at the early (n_{WT} = 6 mice, $n_{R6/2}$ = 9 mice) or mid (n_{WT} = 7 mice, $n_{R6/2}$ = 7 mice) stage of the disease. There was a significant increase in aberrantly spliced *Clcn1* mRNA at the late stage of the disease (n_{WT} = 7 mice, $n_{R6/2}$ = 6 mice; *, P < 0.001). (B and C) Relative percentage of total full-length *Clcn1* mRNA as measured by primers spanning exons 10–14 (B) and exons 16–19 (C). There was no significant difference between WT and R6/2 mice at the early (n_{WT} = 9 mice, $n_{R6/2}$ = 10 mice) or mid (n_{WT} = 9 mice, $n_{R6/2}$ = 10 mice) stage of the disease. There was a significant decrease in total *Clcn1* mRNA at the late-stage of the disease (n_{WT} = 10, $n_{R6/2}$ = 9) for exons 10–14 (*, P = 0.017) and exons 16–19 (*, P < 0.019). (D) Relative pre-mRNA levels measured from late-stage TA muscle and normalized to 18s rRNA from WT (n = 6) and R6/2 (n = 6) mice. There was no significant difference (P = 0.143) between WT (4.901 ± 0.522) and R6/2 (7.967 ± 2.049) *Clcn1* pre-mRNA. Data are presented as mean and errors as SEM.

with WT fibers (Fig. 5 B) as described previously (Waters et al., 2013). Kir channel conductance (G_{Kir}) was the slope of the IV relationship for the peak I_{Kir} from −60 to −40 mV (Fig. 5 C).

To examine the Kir channel defects during disease progression, the G_{Kir} (mS/µF) of individual WT (n = 86 fibers; 25 mice) and R6/2 (n = 90 fibers; 26 mice) skeletal muscle fibers were plotted as a function of age and fit with a linear regression lines (Fig. 6 A). Included are 9 fibers from 4 R6/2 mice and 10 fibers from 3 WT mice from our previous study (Waters et al., 2013). The decrease in R6/2 G_{Kir} over time was not significant (P = 0.138), and R6/2 G_{Kir} was not different relative to WT (P = 0.586). However, G_{Kir} was lower in R6/2 fibers relative to WT fibers throughout the disease progression. Confidence intervals with the mean G_{Kir} per mouse (Fig. 6 B) point to a divergence between WT and R6/2 G_{Kir} at 40 d of age. The apparent divergence of WT and R6/2 G_{Kir}, which was not reflected in the trend lines, may be the result of a smaller sample size for younger mice. Regardless, the data indicate that the R6/2 G_{Kir} began to differ from WT early in muscle maturation.

The age dependence of the relative expression level of full-length Kir mRNA (*Kcnj2*) was also measured. The full-length *Kcnj2* transcripts were significantly reduced (P = 0.005) only in late-stage R6/2 mice relative to WT (Fig. 6 C). Additionally, there was no significant difference in *Kcnj2* pre-mRNA between R6/2 and WT muscle (Fig. 6 D).

Membrane capacitance

Previously, a decrease in the C_m (µF/cm^2) was observed in late-stage R6/2 mice, suggesting a loss of t-tubular membrane in HD skeletal muscle (Waters et al., 2013). The age dependence of C_m was determined from the WT (n = 165 fibers; 56 mice) and R6/2 (n = 167 fibers; 39 mice) fibers used to measure G_{ClC-1} and G_{Kir} (Fig. 7 A). C_m was determined from step changes in voltage-clamp under conditions in which all of the ion channels were blocked (i.e., in the presence of 9AC in the G_{ClC-1} experiments). Fig. 7 includes 14 fibers from 8 R6/2 mice and 19 fibers from 6 WT mice from our previous study (Waters et al., 2013). The C_m of WT fibers did not change with age (P = 0.447), whereas the C_m of R6/2 fibers significantly decreased with age (P < 0.001). Additionally, the WT C_m was significantly different from that of WT over time (P < 0.001). Like G_{ClC-1} and G_{Kir}, the plot of the mean WT and R6/2 C_m values per mouse with confidence intervals (Fig. 7 B) suggests that the divergence between WT and R6/2 C_m occurred at 40 d of age.

The C_m of skeletal muscle depends on fiber diameter, such that smaller fibers have a lower C_m (Hodgkin and Nakajima, 1972). Thus, some of the changes in R6/2 fibers could be caused by disease-related fiber atrophy (Carter et al., 1999; Ribchester et al., 2004; She et al., 2011). To reduce or eliminate this effect, re-

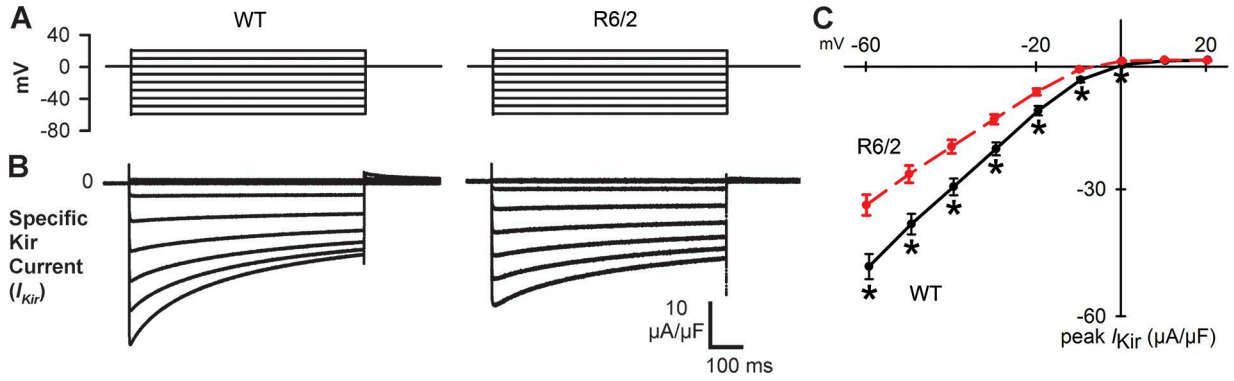

Figure 5. **Kir channel currents.** Mean Kir currents of late-stage WT (n = 38) and R6/2 (n = 18) fibers. (A and B) Voltage-clamp traces for WT (left) and R6/2 (right) fibers. (A) Voltage protocol with a holding potential of 0 mV and a series of 700-ms steps from −60 to 20 mV in 10-mV increments. (B) Specific I_{Kir} values obtained by the method of subtraction. (C) IV relationship of the peak I_{Kir} (mean ± SEM) from B for WT and R6/2 fibers. A significantly lower current (*) was observed from R6/2 mice compared with WT at −60 mV (P = 0.002), −50 mV (P = 0.002), −40 mV (P = 0.002), −30 mV (P = 0.004), −20 mV (P = 0.01), −10 mV (P = 0.005), and 0 mV (P < 0.001), but not at 10 mV (P = 0.071) and 20 mV (P = 0.602). G_{Kir} was the slope of the IV relationship from −40 to −60 mV.

cords were only taken from larger R6/2 fibers in this study. The diameters of all the fibers used for electrophysiology were plotted as a function of age (Fig. S2). There was no difference in diameter between WT and R6/2 fibers at any age (P = 0.191). Thus, the effects of fiber atrophy on C_m was eliminated or greatly minimized by analyzing WT and R6/2 fibers that were similar in size.

Our chloride and potassium current records normalized to capacitance should reflect the current density regardless of any loss of t-tubular membrane. However, a difference between the currents normalized to capacitance or surface area may suggest a loss or altered function in the chloride and potassium channels of the t-tubules. For comparison, the age dependence of $G_{ClC\text{-}1}$ and G_{Kir} normalized to surface area are shown in Fig. S3.

Sequestration of MBNL1

In myotonic dystrophy, type 1, CUG repeats sequester the mRNA-binding protein MBNL1 in nuclear foci of skeletal muscle fibers, which triggers aberrant splicing of several mRNA transcripts (Lin et al., 2006). A combination of IF against MBNL1 and FISH targeting expanded CAG repeats in FDB muscle slices were used to determine whether MBNL1 was similarly sequestered by CAG repeats in late-stage R6/2 skeletal muscle (Fig. 8). MBNL1 and CAG repeat foci were frequently observed in R6/2 muscle; however, those foci rarely colocalized

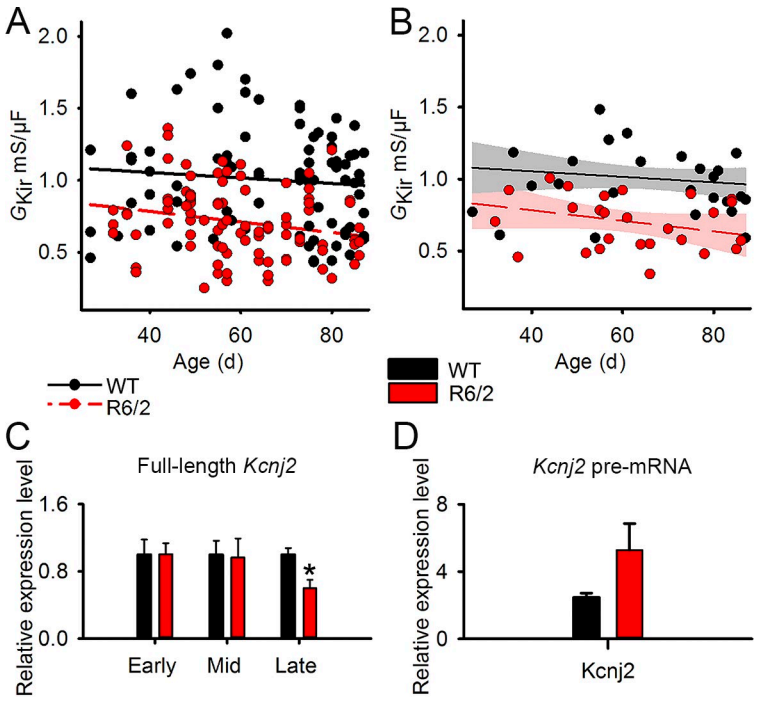

Figure 6. **Age dependence of G_{Kir} and *Kcnj2* mRNA analysis.** (A) G_{Kir} of individual muscle fibers as a function of time. Linear regression lines are shown as solid black lines for WT and broken red lines for R6/2 mice. There was no significant change in R6/2 G_{Kir} over time (P = 0.138), and there was no significant difference between R6/2 and WT slopes (P = 0.586). (B) G_{Kir} of individual mice with 95% confidence intervals for WT (black) and R6/2 (red) mice. The slope of the R6/2 regression line was −0.003 ± 0.002 G_{Kir}/day, and the slope of the WT regression line was −0.001 ± 0.002 G_{Kir}/day. (C) Relative percentage of full-length *Kcnj2* mRNA. There was no significant difference between WT and R6/2 mice at the early (n_{WT} = 9 mice, $n_{R6/2}$ = 10 mice) or mid (n_{WT} = 9 mice, $n_{R6/2}$ = 10 mice) stage of the disease. There was a significant decrease (*) in total *Kcnj2* mRNA at the late stage of the disease (n_{WT} = 10 mice, $n_{R6/2}$ = 9 mice). (D) Relative pre-mRNA levels measured from late-stage TA muscle and normalized to 18s rRNA from WT (n = 6) and R6/2 (n = 6) mice. There was no significant difference (P = 0.080) between WT (2.450 ± 0.269) and R6/2 (5.286 ± 1.574) *Kcnj2* pre-mRNA. Data are presented as mean and errors as SEM.

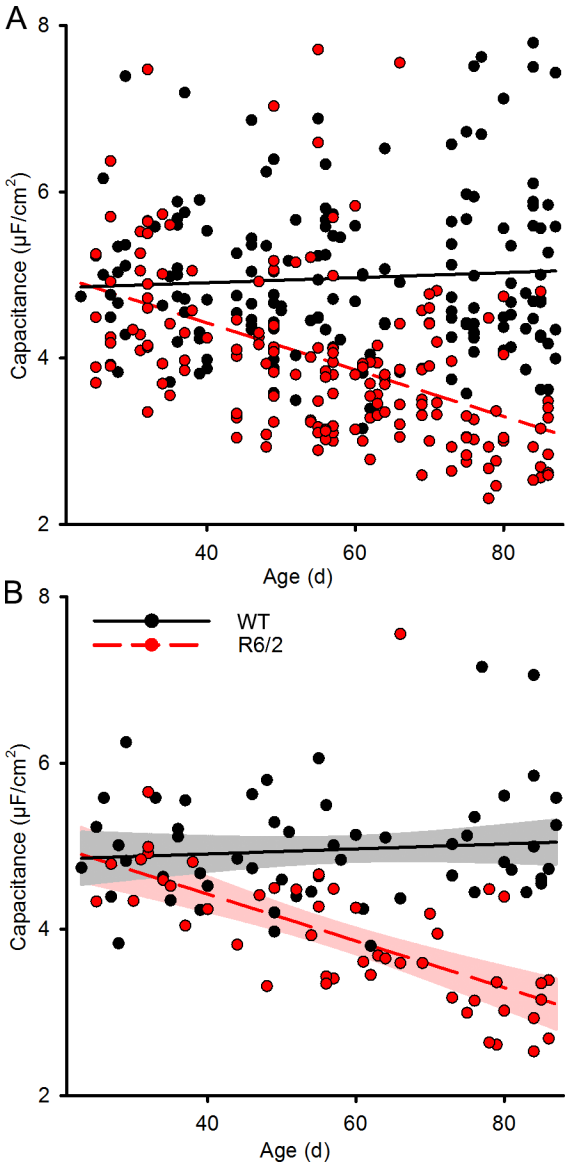

Figure 7. **Age dependence of membrane capacitance (C_m).** (A) The C_m of individual muscle fibers as a function of age with linear regression lines (solid black lines for WT and broken red lines for R6/2 fibers). There was no significant change in WT C_m over time ($P = 0.447$), there was a significant decrease in R6/2 C_m over time ($P < 0.001$), and there was a significant difference between WT and R6/2 slopes ($P < 0.001$). (B) The C_m of individual mice with 95% confidence intervals for WT (black) and R6/2 (red). The slope of the R6/2 regression line was −0.028 ± 0.004 C_m/day, and the slope of the WT regression line was 0.003 ± 0.004 C_m/day.

(Fig. 8 A). Nonetheless, some foci with colocalization were observed but often required searching several slices of muscle tissue to locate (Fig. 8 B). Diffuse MBNL1 immunoreactivity was found throughout the nuclei of R6/2 and WT fibers, which can be seen in the absence of DAPI staining (Fig. 8 B). There was no evidence of MBNL1 or CAG repeat foci in WT nuclei (Fig. 8 C). Cytoplasmic MBNL1 immunoreactivity was observed in both R6/2 and WT fibers, consistent with a previous study of MBNL1 (Wang et al., 2014). Diffuse nuclear labeling of the CAG-trinucleotide repeats in R6/2 fibers and, to a lesser degree, in WT fibers was also detected.

Gastrocnemius muscle slices from HSA^{LR} mice, a model for myotonic dystrophy, type 1, were also examined with the same probes and conditions used for the R6/2 and WT FDB slices. The CAG probe used here has been shown to bind CUG repeats in myotonic dystrophy (Urbanek and Krzyzosiak, 2016). Likewise, CUG probes have been shown to bind CAG repeat expansions in HD (Sun et al., 2015). In contrast to R6/2 tissue, there was abundant colocalization of MBNL1 and CUG repeats (detected by the CAG probe) in nuclear foci of the HSA^{LR} muscle (Fig. 8 D), consistent with a previous study (Urbanek and Krzyzosiak, 2016).

Muscle tissue includes nuclei from multiple cell types, including muscle fibers, endothelial cells, satellite cells, fibroblasts, and other cell types. To confirm specificity to single muscle fibers, the same combination of IF and FISH was performed on dissociated FDB and IO fibers from late-stage R6/2 mice. Consistent with our observations in muscle tissue slices, foci of MBNL1 and the CAG repeats did not colocalize in the nuclei of dissociated fibers (Fig. 8 E).

To determine whether the expression level of MBNL1 was altered in R6/2 tissue, the levels of MBNL1 and MBNL2 were measured by Western blot of whole TA muscle homogenates. No significant changes were found between MBNL1 and MBNL2 protein levels in R6/2 compared with WT (Fig. 9).

MyHC isoform expression

MyHC isoform expression in the TA was assessed in late-stage R6/2 and WT mice. Significant reductions in the expression of MyHC-2x and MyHC-2b, the fastest of the adult MyHC isoforms, were observed at the mRNA level in R6/2 skeletal muscle relative to WT (Fig. 10 A). In contrast, no significant changes in either MyHC-2a or MyHC-1, the slowest adult MyHC isoforms, were observed. MyHC-neonatal mRNA was significantly elevated by a factor of ∼3 in R6/2 compared with WT mice ($P = 0.008$). Although MyHC-embryonic mRNA was not significantly different between WT and R6/2 skeletal muscle ($P = 0.135$), the level of MyHC-embryonic tended to be higher in R6/2 mice relative to WT. Curiously, at the protein level (Fig. 10 B), it was found that MyHC-2x was elevated in R6/2 mice relative to WT ($P = 0.004$). Embryonic and neonatal MyHC proteins were not clearly observed in the SDS-PAGE gels of WT and R6/2 TA muscle, which may have occurred because of co-migration of neonatal MyHC with MyHC-2x and co-migration of embryonic with MyHC-2a. Expressing the mRNA data as mean expression level relative to β2-microglobulin (but not normalized per isoform) reveals that the magnitude of the reduction in MyHC-2b

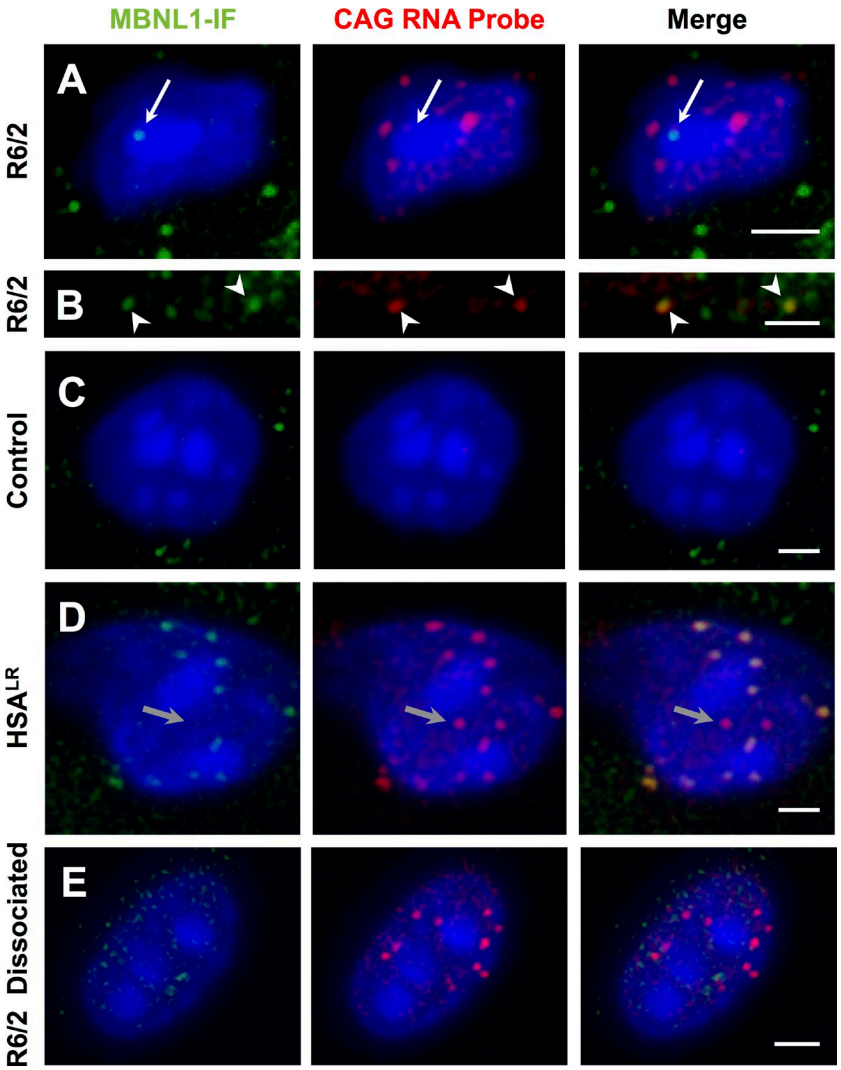

Figure 8. **Sequestration of MBNL1 and CAG repeats in late-stage R6/2 skeletal muscle nuclei.** MBNL1 IF (MBNL1-IF; green) and fluorescent-labeled CAG in situ hybridization (CAG RNA Probe; red) in the nuclei (DAPI; blue) of R6/2, WT, and HSA^{LR} muscle (HSA^{LR} is a model of myotonic dystrophy, type 1). All micrographs were confocal stacks (10 optical sections, z = 0.3 µm) imaged with conserved parameters. Bars, 2 µm. (A) MBNL1 (white arrows) and CAG repeats formed nuclear foci in whole R6/2 FDB muscle tissue slices but frequently did not colocalize. (B) Some nuclear foci contain colocalized MBNL1 and CAG repeats (white arrowheads). In the absence of DAPI, diffuse/low intensity staining of MBNL1 in R6/2 nuclei was observed. (C) Little to no nuclear foci of MBNL1 and CAG were observed in WT FDB tissue. Diffuse labeling of MBNL1 and the CAG repeats was observed in WT nuclei not obscured by DAPI staining (not depicted). (D) Extensive colocalization of MBNL1 and the CAG probe was observed in HSA^{LR} gastrocnemius tissue. A small number of non-colocalized foci were also present (gray arrows). Note that CAG probe binds CUG repeats in the HSA^{LR} slices; such cross-reactivity has been shown previously (Sun et al., 2015; Urbanek and Krzyzosiak, 2016). (E) Dissociated FDB fibers from R6/2 mice were probed for CAG repeat and MBNL1 sequestration to confirm that the observations made in whole muscle sections (with many cell types) were specific to muscle fiber nuclei.

was significantly greater than the reduction in MyHC-2x mRNA (Fig. 10 C). This resulted in an elevation in the total proportion of MyHC-2x mRNA in R6/2 mice relative to WT (Fig. 10 D), which corresponded to the net increase in MyHC-2x protein. This, in part, explains the increase in MyHC-2x at the protein level despite an absolute reduction at the mRNA level because the proportion of MyHC isoforms synthesized at the protein level (Fig. 10 B) likely reflects the proportions at the mRNA level (Fig. 10 D).

Q175 mice

To show that the altered maturational state observed in HD skeletal muscle was not unique to the early-onset model for HD (i.e., the R6/2 mouse model), $G_{ClC\text{-}1}$, C_m, *Clcn1* mRNA processing, and MyHC isoform expression were measured in another model for HD, the Q175 mouse line (a model for late onset of HD symptoms), and their WT littermates. 1-yr-old (12–15 mo) Q175 HD mice (n = 25 fibers; 4 mice) and age-matched WT mice (n = 21 fibers; 3 mice) were analyzed. When normalized to capacitance, there was a significant difference between Q175 (1.1 ± 0.1 mS/µF) and WT (1.4 ± 0.1 mS/µF) $G_{ClC\text{-}1}$ (P = 0.013). There was also a significant difference between Q175 (4.3 ± 0.4 mS/cm^2) and WT (7.3 ± 0.6 mS/cm^2) $G_{ClC\text{-}1}$ if normalized to surface area (P < 0.001). A significant difference between Q175 (3.9 ± 0.1 µF/cm^2) and WT (5.1 ± 0.1 µF/cm^2) C_m (P < 0.001) was also observed.

In addition to $G_{ClC\text{-}1}$, changes in *Clcn1* mRNA aberrant splicing were also observed in Q175 mice. These changes were similar to those observed in R6/2 mice (Fig. 11 A). Whereas FDB and IO muscles were removed and dissociated for single fiber electrophysiological experiments, TA muscles were removed from the same Q175 (n = 5 mice) and WT (n = 5) mice for mRNA analysis. A significant increase (P = 0.05) in aberrantly spliced *Clcn1* mRNA containing exon 7a was observed in Q175 skeletal muscle (7.20 ± 0.32% misspliced) compared with WT mice (6.02 ± 0.48% misspliced). However, no differences were observed in full-length *Clcn1* mRNA.

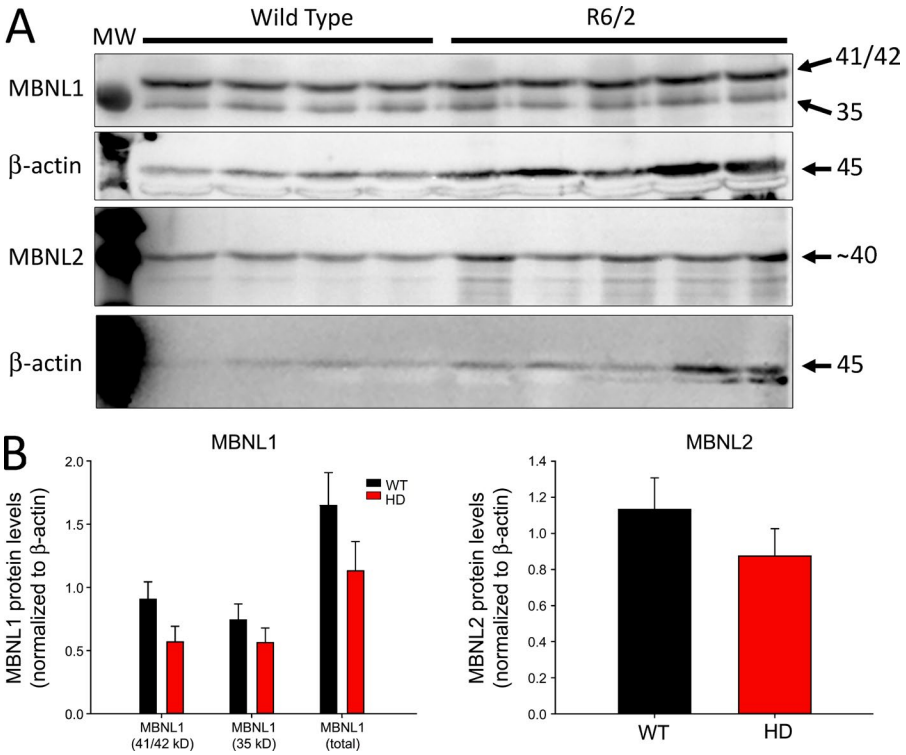

Figure 9. **MBNL protein levels.** Protein levels of MBNL1 and MBNL2 were measured from late-stage TA muscle from WT (n = 6) and R6/2 (n = 6) mice. (A and B) Western blot analysis (A) shows no significant difference (B) between WT and R6/2 mice for the 41/42-kD variant of MBNL1 (P = 0.331), the 35-kD variant of MBNL1 (P = 0.825), or MBNL2 (P = 0.373). Data are presented as mean and errors as SEM.

Similar to the R6/2 mouse model of HD, the Q175 mice showed a significant reduction (P = 0.008) in MyHC-2b mRNA (Fig. 11 B). Although significant changes were not detected in MyHCs-1, -2a, -2x, or -embryonic, the neonatal MyHC isoform tended to be elevated, although not significantly (P = 0.08).

DISCUSSION

Previously, we found defects in R6/2 skeletal muscle $I_{ClC\text{-}1}$ and I_{Kir}, membrane capacitance, and mRNA processing (Waters et al., 2013). The resulting hyperexcitability causes delayed muscle relaxation that can help explain the dystonia, rigidity, and bradykinesia that characterize the motor symptoms of HD. However, all of this previous work was completed with R6/2 mice that were near terminal. Thus, the initial objective of this study was to determine the time course over which these defects develop in R6/2 mice. It was found that the skeletal muscle defects present before motor symptom onset and that the ClC-1 defects increased in severity throughout disease progression. This lead to the discovery of neonatal MyHC isoforms expression in both juvenile-onset (R6/2) and adult-onset (Q175) HD mouse models. Finally, despite similar deficits in chloride currents and *Clcn1* mRNA splicing, we report evidence that the underlying mechanism for these deficits may, in large part, be unique from that observed in myotonic dystrophy, type 1.

Weight loss, muscle growth, and behavior

It is well known that R6/2 mice lose weight with age (Carter et al., 1999; Ribchester et al., 2004; She et al., 2011), in part, as a result of disease-related skeletal muscle atrophy (Mielcarek et al., 2015). Our results show a plateau in R6/2 mouse weight from 6 to 10 wk of age, a lack of growth that may be related to a disruption in muscle maturation. The weight loss that began at 10 wk of age in R6/2 mice can be attributed primarily to atrophy, suggesting that muscle atrophy predominates at the late stage of the disease rather than a lack of growth. This corresponds to an analysis of R6/2 muscle fiber diameter that showed decreases in diameter beginning after 8 wk of age (Ribchester et al., 2004).

In our previous study of R6/2 mouse home cage activity (Steele et al., 2007), decreases in locomotor and exploratory behaviors were notable even in early stages of disease and steadily declined thereafter. In the present study, we observed similar levels of most locomotor behaviors and only observed a decrease in hanging behavior at the last time point tested. Given that the sample sizes used for behavioral measurements were low, it is difficult to conclude whether the R6/2 home cage behavioral phenotype has changed over the past decade or whether we happened to use several mice that were less affected by the disease transgene. Further testing of locomotor behaviors and grip strength may be warranted to determine how well the alterations in muscle physiology and transcription correlate to gross locomotor phenotypes in the R6/2 mice.

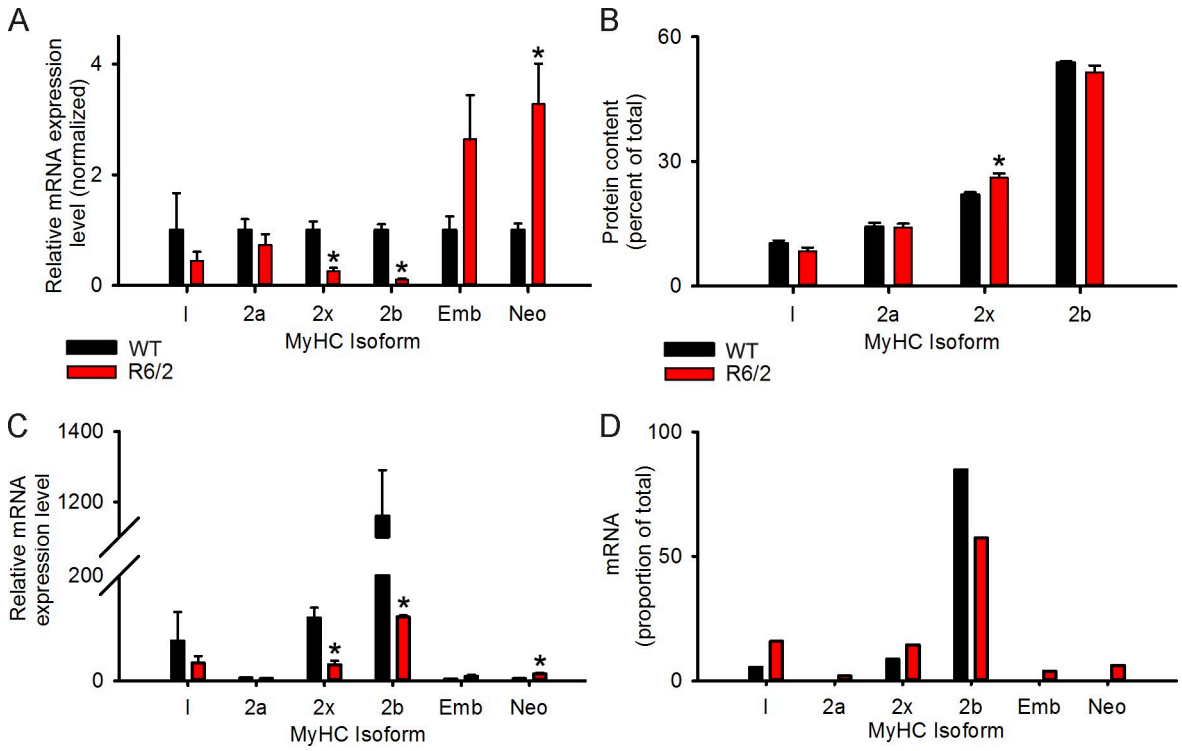

Figure 10. **MyHC isoform expression.** (A) MyHC isoform mRNA levels in WT and R6/2 TA muscle. Values were normalized to the WT expression level for a given isoform. The 2x and 2b isoforms were reduced in R6/2 muscle compared with WT. In contrast, the neonatal isoform was significantly elevated in R6/2 mice. Although not statistically different, the embryonic isoform was trending to be elevated in R6/2 muscle. *, $P < 0.05$. (B) Protein levels of MyHC-1, MyHC-2a, MyHC-2b, and MyHC-2x were measured from late-stage TA muscle from WT ($n = 5$) and R6/2 ($n = 5$) mice. There was a significantly higher (*, $P = 0.004$) level of MyHC-2x in R6/2 mice compared with WT and no significant difference in MyHC-1 ($P = 0.075$), MyHC-2a ($P = 0.948$), or MyHC-2b ($P = 0.159$) protein levels. Possibly because of comigration with 2x, the neonatal isoform was not clearly identified. (C) Mean relative MyHC isoform mRNA levels in WT and R6/2 mice (not normalized for a given isoform). As expected, MyHC isoforms 2b and 2x were the predominant MyHC isoforms expressed in the TA of WT and R6/2 mice. *, $P < 0.05$. (D) Proportions of each MyHC isoform relative to the total of all isoforms as calculated from the mean relative MyHC isoform levels. The absolute magnitude of the reduction in MyHC-2b mRNA was greater than the absolute magnitude of the reduction in MyHC-2x mRNA. Thus, when expressing the data as the proportion of a given mRNA isoform for WT and R6/2 (D), an increase in the proportion of MyHC-2x isoform mRNA was observed in R6/2 mice. Data are presented as mean and errors as SEM.

ClC-1 defects

In support of disrupted muscle maturation, R6/2 $G_{ClC\text{-}1}$ remained constant over the time course of the disease, whereas WT $G_{ClC\text{-}1}$ steadily increased. Changes in *Clcn1* mRNA alternative splicing followed the same age-dependent trend. Namely, *Clcn1* mRNA containing exon 7a remained constant over the time course of the disease. In WT muscle, however, high levels of aberrantly spliced *Clcn1* mRNA were observed early in the time course and progressively decreased with age. This observation is consistent with other studies showing postnatal decrease of *Clcn1* mRNA containing exon 7a (Pierno et al., 1999; Mankodi et al., 2002; Lin et al., 2006). The inclusion of exon 7a results in a frame shift and premature termination of ClC-1 translation, resulting in fewer channel proteins. In addition to the exon 7a inclusion, a significant increase in late-stage R6/2 *Clcn1* mRNA splice variants (spanning exons 5–8) that are normally expressed in WT neonatal muscle (Mankodi et al., 2002) was observed. Thus, taking into account the reduction in full-length *Clcn1* mRNA and normal levels of *Clcn1* pre-mRNA, our data support a reduction in *Clcn1* mRNA expression through processing defects that underlie the progressive reduction in $G_{ClC\text{-}1}$ in addition to an altered transition from neonatal to adult mRNA splicing in R6/2 skeletal muscle.

Kir channels

Previously, we showed that G_{Kir} is reduced in late-stage R6/2 skeletal muscle. Together, the decreased G_{Kir} and $G_{ClC\text{-}1}$ in late-stage R6/2 mice causes muscle hyperexcitability. Here, we found that the R6/2 G_{Kir} remained consistently lower than WT throughout the progression of the disease. This indicates that there is a very early or persistent decrease in R6/2 G_{Kir} that may contribute to the motor symptoms throughout the majority of disease progression.

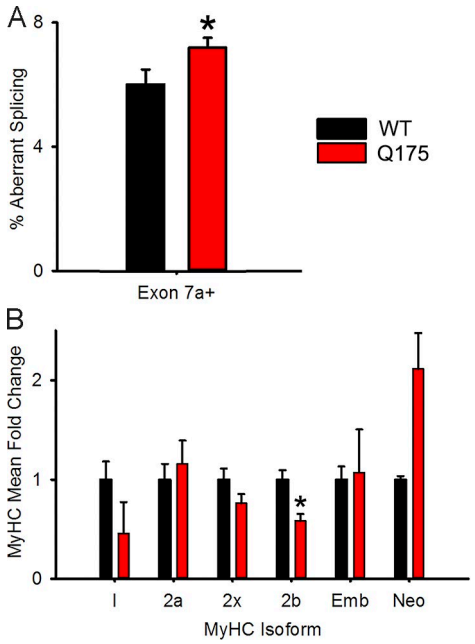

Figure 11. **Q175 mouse mRNA analysis.** (A) Percentage of *Clcn1* mRNA with inclusion of exon 7a relative to total. There was a significantly higher level of *Clcn1* aberrant splicing in Q175 TA (n = 5) muscle compared with WT (n = 5; *, P = 0.05). (B) There was a significantly lower level of the MyHC 2b isoform in Q175 TA muscle compared with WT (*, P = 0.008), but no significant change in other MyHC isoforms (n = 5 per group). Data are presented as mean and errors as SEM.

Unlike the parallel progression of G_{Kir}, the levels of full-length *Kcnj2* mRNA decreased markedly in late-stage R6/2 muscle compared with WT. This reduction is most likely caused by a posttranscriptional processing event other than aberrant splicing because (a) no significant changes in *Kcnj2* pre-mRNA levels were observed in late-stage R6/2 skeletal muscle, and thus transcription appears to be unaffected; and (b) the structure of the *Kcnj2* gene includes only a single intron, and previous work found no evidence of alternative splicing of this gene (Houtman et al., 2012). Possible explanations for the decrease in full-length *Kcnj2* mRNA in late-stage R6/2 muscle include alterations in mRNA transcript stability, altered expression of regulatory miRNAs, or altered expression of natural antisense transcripts. Additionally, an up-regulation of other Kir channel isoforms in late-stage R6/2 muscle may compensate for the drop in full-length *Kcnj2* mRNA, which codes for the Kir2.1 isoform. Future analyses of the Kir channel protein will be needed to gain a greater understanding of the changes in Kir channel function that occur in R6/2 skeletal muscle.

Membrane capacitance

Our analysis of the C_m may provide insights into the morphology of the R6/2 muscle fibers. Fiber capacitance is proportional to the total amount of extracellular membrane, which in skeletal muscle includes the sarcolemma and the t-tubular membrane. Assuming all the extracellular membrane is included in the surface area estimate, the C_m would be ~1 μF/cm^2, the typical capacitance of a biological membrane. Mature mammalian skeletal fibers have a C_m of ~5 μF/cm^2 because estimates of surface area do not include the internal t-tubular system (Falk and Fatt, 1964). Thus, a likely explanation for the R6/2 fibers having a lower C_m compared with WT mice is a loss or disruption of t-tubular membrane in the disease fibers. Such a t-tubular membrane defect would reduce the Ca^{2+} released per action potential and help explain the muscle weakness that is common in HD patients. Indeed, reduced Ca^{2+} transients have recently been measured in HD skeletal muscle fibers (Braubach et al., 2014). Future experiments will be needed to directly assess the amount of t-tubular membrane in HD fibers and correlate those measurements with intracellular Ca^{2+} levels and specific force generation.

In this study, it is shown that the reduction in C_m of R6/2 fibers compared with WT mice increases with disease progression. Similar to the age-dependent changes in G_{ClC-1} and aberrantly spliced *Clcn1* mRNA levels, the C_m of R6/2 skeletal muscle fibers began to diverge from WT mice in ~5-wk-old mice. In contrast, the C_m of WT fibers were stable over the 3- to 12-wk age range. This data indicates an increasing disruption of membrane structure in R6/2 skeletal muscle during disease progression.

The total fiber capacitance was used to normalize our I_{ClC-1} and I_{Kir}, which provides a measure of current density, regardless of the amount of t-tubular membrane. The same currents normalized to fiber surface area (Fig. S3) show more dramatic age-dependent differences between WT and R6/2 fibers. A straightforward explanation for this is that ClC-1 and Kir channels are being lost along with t-tubular membrane. If the loss of t-tubular membrane is confirmed by direct optical measurements, these results have implications for the uncertainty on whether or not ClC-1 is expressed in the t-tubules (Lueck et al., 2010; DiFranco et al., 2011).

MyHC isoform expression in R6/2 mice

To test for disrupted muscle maturation, the profile of MyHC isoform expression was examined in late-stage WT and R6/2 skeletal muscle. Identifying MyHC isoforms is an established method for assessing changes in the phenotypic properties of muscle (Billeter et al., 1981; Talmadge and Roy, 1993). As expected, little neonatal and embryonic myosin mRNA were present in late-stage WT skeletal muscle. However, a threefold increase in the expression of MyHC-neonatal in the TA of late-stage R6/2 mice was observed, indicating that the

fast TA muscle either retains or re-attains some characteristics of a developing muscle.

Most fiber type analyses of mature skeletal muscle focus on fiber types 1 and 2. Type 1 fibers express MyHC-1 and have a slow time-to-peak tension, slow maximal shortening velocity, and a high capacity for oxidative metabolism that results in a high resistance to fatigue. Type 2 fibers generally have faster time-to-peak tensions and a range of oxidative capacities generally resulting in less resistance to fatigue (Talmadge, 2000; Schiaffino and Reggiani, 2011). Based on MyHC isoform content, type 2 fibers may be further subdivided into types 2a (MyHC-2a), 2d/x (MyHC-2x), and 2b (MyHC-2b) in mice. Type 2a, 2d/x, and 2b fibers are high, intermediate, and low in oxidative capacity, respectively, with a corresponding reduction in resistance to fatigue. A transition from type 2x or 2b to the more oxidative type 2a can occur normally with increased contractile activity as may occur with endurance training (Pette and Vrbová, 1992). Previous studies suggest that R6/2 fibers become more oxidative (Ribchester et al., 2004; Strand et al., 2005; Mielcarek et al., 2015). This could be because of the hyperexcitability of R6/2 muscle fibers causing an increase in contractile activity and a subsequent transition in fiber type from 2b toward 2x or 2a. Indeed, in the R6/2 mice, there was a pronounced reduction in the expression of the fastest MyHC-2b isoform (see Fig. 10 C). This resulted in an elevation in the relative proportion of MyHC-1 and MyHC-2x mRNA proportions (see Fig. 10 D). Thus, the TA muscle of R6/2 mice appears to be undergoing a fast to slow shift, resulting from a dominant down-regulation in fast MyHC-2b isoform expression. These molecular changes would support the physiological data showing a decreased time-to-peak tension and maximal shortening velocity in R6/2 mice compared with WT (Mielcarek et al., 2015). In apparent contrast, Chaturvedi et al. (2009) reported that R6/2 muscles showed an elevation in the expression MyHC-2b and a reduction in MyHC-1 consistent with a slow to fast shift in fiber type. However, these data were obtained from the slow soleus muscle, not the fast TA muscle used in this study. In addition, the expression of MyHC isoforms normally expressed during development were not assessed by Chaturvedi et al. (2009). If skeletal muscles in R6/2 mice were less mature than WT, it might be expected that the muscles would acquire an intermediate fiber phenotype, such that fast muscles (like the TA) would be slower (current data) and slow muscles (like the soleus) would be faster (Chaturvedi et al., 2009) than WT.

In Q175 mice, the trend toward higher levels of neonatal MyHC was particularly striking given that they were 12–15 mo old. This suggests that there may be a possible down-regulation of MyHC-2b with a corresponding up-regulation of MyHC-neonatal, both of which are alternatively regulated. Normally, MyHC-2b is up-regulated during maturation and MyHC-neonatal is down-regulated, further supporting a disruption in HD skeletal muscle maturation. The Q175 data also suggest that a shift to isoforms normally expressed in earlier developmental states is relevant to adult-onset HD.

In total, the different conclusions regarding R6/2 fiber type transitions may be explained by the persistence of or a reversion toward a neonatal fiber type, as suggested by the presence of mRNA for neonatal myosin. Thus, a disruption of muscle maturation could partially explain these disparities.

The disruption in skeletal muscle maturation reported here may be similar to the lack of neurogenesis found in the hippocampus of HD mouse models and HD patients (Gil et al., 2005; Orvoen et al., 2012). Moreover, a lack of growth, rather than degeneration of striatal neurons, has been observed in R6/2 mice (Rattray et al., 2013). Similar observations have been made in other tissues such as the pancreas in HD (Björkqvist et al., 2005). Because of its abundance and high accessibility, skeletal muscle may prove to be a very useful model for better understanding the changes in HD developmental states.

Relation to juvenile- and adult-onset HD

Analogous to R6/2 mice, the onset of overt symptoms in human juvenile-onset HD patients coincides with muscle maturation during adolescence. Perhaps surprisingly, this disruption in muscle maturation appears relevant to adult-onset HD. We found reduced $G_{ClC\text{-}1}$ and increased aberrantly spliced *Clcn1* mRNA in skeletal muscle from the Q175 mice, a model for adult-onset HD. The mean $G_{ClC\text{-}1}$ value of 1-yr-old Q175 mice (1.1 ± 0.1 mS/µF) reported here was similar to that of 12-wk-old near-terminal R6/2 mice (1.0 ± 0.1 mS/µF), as we reported previously (Waters et al., 2013). However, the mean $G_{ClC\text{-}1}$ value of 1-yr-old WT Q175 littermates (1.4 ± 0.1 mS/µF) was substantially lower than that of 12-wk-old WT R6/2 littermates (2.4 ± 0.1 mS/µF), suggesting that $G_{ClC\text{-}1}$ may normally decrease with age. Strikingly, high levels of neonatal myosin in the 1-yr-old Q175 mice were also observed. The Q175 data suggest that a reversion to earlier developmental states may occur in adult-onset HD. A time course study with the Q175 mice or another late-onset model will be needed to better address muscle changes in adult HD.

Nuclear sequestration of MBNL1

For the first time in adult R6/2 skeletal muscle, we show abnormal nuclear sequestration of MBNL1 protein without predominate colocalization with CAG foci. It is unlikely that the threshold for detecting MBNL1 at the CAG repeat foci was low because small punctae of MBNL1 immunoreactivity were detectable

throughout the tissue. Our data suggest that a novel mechanism in addition to MBNL1 sequestration by CAG repeats may underlie the aberrant splicing of *Clcn1* mRNA in R6/2 skeletal muscle. Nonetheless, the pathology likely involves MBNL1 because abnormal aggregates of MBNL1 were present in R6/2 muscle nuclei, and previous studies have shown colocalized MBNL1 and CAG repeats in fibroblasts and other in vitro systems of HD, including those that overexpress MBNL1 (de Mezer et al., 2011; Sun et al., 2015). Future investigations will need to examine other RNA-binding factors in R6/2 muscle, such as the CELF family of proteins that includes the CUG-binding protein, CUGBP, and embryonically lethal abnormal vision-type RNA-binding protein 3, ETR-3 (Ladd et al., 2001; Lin et al., 2006; Lee et al., 2013). The identity of the proteins involved in the mRNA processing defects may depend on the age of the muscle.

Denervation

The phenotype of R6/2 skeletal muscle has been described as denervation like (Ribchester et al., 2004), and a recent study has further suggested that motor unit loss and denervation drive the changes in muscle excitability by measuring changes in muscle contractility during step changes in motor neuron excitation (Mielcarek et al., 2015). Contradicting the denervation idea is that a morphological analysis of R6/2 mouse neuromuscular junctions showed defects in only a very small fraction of neuromuscular junctions (Ribchester et al., 2004). A more recent study has also reported morphological changes, including vesicle shape at the neuromuscular junction of R6/2 mice, but showed no clear evidence of denervation (de Aragão et al., 2016). Moreover, re-innervation after crushing the motor neuron was normal in R6/2 skeletal muscle (Ribchester et al., 2004). The results of our study are also not easy to reconcile with denervation, or at least significant denervation. Denervation would need to occur before 5 wk of age in the R6/2 mice and cause no symptoms in order to drive the muscle defects observed. Perhaps the changes in muscle contractility with varying nerve stimulation recently reported (Mielcarek et al., 2015) were the result of motor neuron hyperexcitability, as has been observed in skeletal muscle in this article and previously (Waters et al., 2013) and in striatal neurons (Ariano et al., 2005). Alternatively, changes in muscle fiber types and/or motor neuron functional characteristics could contribute to the changes in contractility. Ultimately, a functional examination of neuromuscular transmission, under voltage-clamp conditions (to eliminate the effects caused by changes in passive muscle membrane properties) will be needed to determine the contribution of any presynaptic defects to HD skeletal muscle.

Conclusion

Our findings demonstrate the presence of progressive skeletal muscle defects that begin before the onset of motor symptoms in R6/2 mice. We also made the novel observation that there is a disruption in muscle maturation, as indicated by the elevation in neonatal MyHC mRNA and a developmental *Clcn1* mRNA splice variant in both R6/2 and Q175 models of HD. Additionally, we show that the mRNA processing defects in R6/2 mice may be distinct from what has been demonstrated in myotonic dystrophy, type 1. The aberrant splicing of gene transcripts has been observed in HD patients (Lin et al., 2016) as well as patients with fragile x-associated tremor/ataxia syndrome (Sellier et al., 2010), another trinucleotide repeat disease. In both diseases, the splicing defects were found in brain tissue, suggesting that the defects in R6/2 skeletal muscle are applicable to multiple tissues and humans.

The results reported herein support that HD is a myopathy in addition to a neurodegenerative disease and may provide a new opportunity to improve patient care by targeting skeletal muscle tissue. Current methods for assessing HD progression in patients involve costly MRI and PET scans (Niccolini et al., 2015). Because of their early presentation, these defects in skeletal muscle may serve as highly accessible biomarkers of disease. In addition to biomarkers, new therapeutic targets can be developed to decrease hyperexcitability in HD skeletal muscle. For example, retigabine, which activates potassium channels (KCNQ) and reduces hyperexcitability, has been shown to improve locomotor activity in R6/2 mice (Cao et al., 2015). In addition to acting on striatal neurons, retigabine may improve locomotor function by reducing hyperexcitability in skeletal muscle. Although CNS dysfunction is the primary target for current therapeutic strategies, the results in this study highlight that HD is a multi-system disease and justifies the necessity for more systemic approaches to cure and/or delay HD symptoms.

ACKNOWLEDGEMENTS

We thank Mrs. Cynthia Tessler for helping oversee animal care at California State Polytechnic University, Pomona. We thank Dr. Donald Loo (David Geffen School of Medicine at UCLA) for editorial comments. For the valuable MBNL1 antibody as well as the HSA^{LR} tissue, we thank Dr. Charles Thornton. The antibodies used to detect MBNL1 and MBNL2 proteins in Western blots (MB1a(4A8) and MB2a(3B4)) were developed by Dr. Glenn E. Morris. These antibodies were obtained from the Developmental Studies Hybridoma Bank, which was created by the Eunice Kennedy Shriver National Institute of Child Health and Human Development of the National Institutes of Health and maintained at The University of Iowa, Department of Biology, Iowa City, IA. Last, but not least, we would like to thank Roger Cachope and the CHDI (New York, NY) for their generous gift, the Q175 mice and their WT littermates.

This work was supported by National Institutes of Health/National Institute of General Medical Sciences grant 1SC3GM096945

and Wright State University startup funds to A.A. Voss. Additionally, D.R. Miranda was supported by the Wright State University Biomedical Sciences PhD Program.

The authors declare no competing financial interests.

Author contributions: Conception and design of the work: V. Bahn, A.D. Steele, R.J. Talmadge, and A.A. Voss. Acquisition, analysis, or interpretation of data for the work: D.R. Miranda, M. Wong, S.H. Romer, C. McKee, G. Garza-Vasquez, A.C. Medina, V. Bahn, A.D. Steele, R.J. Talmadge, and A.A. Voss. Drafting the work or revising it critically for important intellectual content: D.R. Miranda, M. Wong, S.H. Romer, C. McKee, G. Garza-Vasquez, A.C. Medina, V. Bahn, A.D. Steele, R.J. Talmadge, and A.A. Voss. All authors approved the final version of this manuscript and agree to be accountable for all aspects of the work. All persons designated as authors qualify for authorship, and all those who qualify for authorship are listed.

Eduardo Ríos served as editor.

Submitted: 7 April 2016
Revised: 3 October 2016
Accepted: 16 November 2016

REFERENCES

Ariano, M.A., C. Cepeda, C.R. Calvert, J. Flores-Hernández, E. Hernández-Echeagaray, G.J. Klapstein, S.H. Chandler, N. Aronin, M. DiFiglia, and M.S. Levine. 2005. Striatal potassium channel dysfunction in Huntington's disease transgenic mice. *J. Neurophysiol.* 93:2565–2574. http://dx.doi.org/10.1152/jn.00791.2004

Bates, G., P.S. Harper, and L. Jones, editors. 2002. Huntington's Disease. Third edition. Oxford University Press, Oxford. 558 pp.

Bezanilla, F., J. Vergara, and R.E. Taylor. 1982. Voltage Clamping of Excitable Membranes. *In* Methods in Experimental Physics. G. Ehrenstein, and H. Lecar, editors. Academic Press, Cambridge, MA. 445–511.

Billeter, R., C.W. Heizmann, H. Howald, and E. Jenny. 1981. Analysis of myosin light and heavy chain types in single human skeletal muscle fibers. *Eur. J. Biochem.* 116:389–395. http://dx.doi.org/10.1111/j.1432-1033.1981.tb05347.x

Björkqvist, M., M. Fex, E. Renström, N. Wierup, A. Petersén, J. Gil, K. Bacos, N. Popovic, J.Y. Li, F. Sundler, et al. 2005. The R6/2 transgenic mouse model of Huntington's disease develops diabetes due to deficient β-cell mass and exocytosis. *Hum. Mol. Genet.* 14:565–574. http://dx.doi.org/10.1093/hmg/ddi053

Bradford, M.M. 1976. A rapid and sensitive method for the quantitation of microgram quantities of protein utilizing the principle of protein-dye binding. *Anal. Biochem.* 72:248–254. http://dx.doi.org/10.1016/0003-2697(76)90527-3

Braubach, P., M. Orynbayev, Z. Andronache, T. Hering, G.B. Landwehrmeyer, K.S. Lindenberg, and W. Melzer. 2014. Altered Ca^{2+} signaling in skeletal muscle fibers of the R6/2 mouse, a model of Huntington's disease. *J. Gen. Physiol.* 144:393–413. http://dx.doi.org/10.1085/jgp.201411255

Busse, M.E., G. Hughes, C.M. Wiles, and A.E. Rosser. 2008. Use of hand-held dynamometry in the evaluation of lower limb muscle strength in people with Huntington's disease. *J. Neurol.* 255:1534–1540. http://dx.doi.org/10.1007/s00415-008-0964-x

Cao, Y., D. Bartolomé-Martín, N. Rotem, C. Rozas, S.S. Dellal, M.A. Chacon, B. Kadriu, M. Gulinello, K. Khodakhah, and D.S. Faber. 2015. Rescue of homeostatic regulation of striatal excitability and locomotor activity in a mouse model of Huntington's disease. *Proc. Natl. Acad. Sci. USA.* 112:2239–2244. http://dx.doi.org/10.1073/pnas.1405748112

Carter, R.J., L.A. Lione, T. Humby, L. Mangiarini, A. Mahal, G.P. Bates, S.B. Dunnett, and A.J. Morton. 1999. Characterization of progressive motor deficits in mice transgenic for the human Huntington's disease mutation. *J. Neurosci.* 19:3248–3257.

Chaturvedi, R.K., P. Adhihetty, S. Shukla, T. Hennessy, N. Calingasan, L. Yang, A. Starkov, M. Kiaei, M. Cannella, J. Sassone, et al. 2009. Impaired PGC-1α function in muscle in Huntington's disease. *Hum. Mol. Genet.* 18:3048–3065. http://dx.doi.org/10.1093/hmg/ddp243

Chomczynski, P., and N. Sacchi. 1987. Single-step method of RNA isolation by acid guanidinium thiocyanate-phenol-chloroform extraction. *Anal. Biochem.* 162:156–159. http://dx.doi.org/10.1016/0003-2697(87)90021-2

de Aragão, B.C., H.A. Rodrigues, P.A. Valadão, W. Camargo, L.A. Naves, F.M. Ribeiro, and C. Guatimosim. 2016. Changes in structure and function of diaphragm neuromuscular junctions from BACHD mouse model for Huntington's disease. *Neurochem. Int.* 93:64–72. http://dx.doi.org/10.1016/j.neuint.2015.12.013

de Mezer, M., M. Wojciechowska, M. Napierala, K. Sobczak, and W.J. Krzyzosiak. 2011. Mutant CAG repeats of Huntingtin transcript fold into hairpins, form nuclear foci and are targets for RNA interference. *Nucleic Acids Res.* 39:3852–3863. http://dx.doi.org/10.1093/nar/gkq1323

DiFranco, M., A. Herrera, and J.L. Vergara. 2011. Chloride currents from the transverse tubular system in adult mammalian skeletal muscle fibers. *J. Gen. Physiol.* 137:21–41. http://dx.doi.org/10.1085/jgp.201010496

Ehrnhoefer, D.E., N.H. Skotte, S. Ladha, Y.T. Nguyen, X. Qiu, Y. Deng, K.T. Huynh, S. Engemann, S.M. Nielsen, K. Becanovic, et al. 2014. p53 increases caspase-6 expression and activation in muscle tissue expressing mutant huntingtin. *Hum. Mol. Genet.* 23:717–729. http://dx.doi.org/10.1093/hmg/ddt458

Falk, G., and P. Fatt. 1964. Linear electrical properties of striated muscle fibres observed with intracellular electrodes. *Proc. R. Soc. Lond. B Biol. Sci.* 160:69–123. http://dx.doi.org/10.1098/rspb.1964.0030

Gil, J.M.A.C., P. Mohapel, I.M. Araújo, N. Popovic, J.-Y. Li, P. Brundin, and A. Petersén. 2005. Reduced hippocampal neurogenesis in R6/2 transgenic Huntington's disease mice. *Neurobiol. Dis.* 20:744–751. http://dx.doi.org/10.1016/j.nbd.2005.05.006

Hodgkin, A.L., and S. Nakajima. 1972. The effect of diameter on the electrical constants of frog skeletal muscle fibres. *J. Physiol.* 221:105–120. http://dx.doi.org/10.1113/jphysiol.1972.sp009742

Holt, I., V. Jacquemin, M. Fardaei, C.A. Sewry, G.S. Butler-Browne, D. Furling, J.D. Brook, and G.E. Morris. 2009. Muscleblind-like proteins: Similarities and differences in normal and myotonic dystrophy muscle. *Am. J. Pathol.* 174:216–227. http://dx.doi.org/10.2353/ajpath.2009.080520

Houtman, M.J.C., H. Takanari, B.G.J.M. Kok, M. van Eck, D.R. Montagne, M.A. Vos, T.P. de Boer, and M.A.G. van der Heyden. 2012. Experimental mapping of the canine *KCNJ2* and *KCNJ12* gene structures and functional analysis of the canine $K_{IR}2.2$ ion channel. *Front. Physiol.* 3:9. http://dx.doi.org/10.3389/fphys.2012.00009

Huey, K.A., F. Haddad, A.X. Qin, and K.M. Baldwin. 2003. Transcriptional regulation of the type I myosin heavy chain gene in denervated rat soleus. *Am. J. Physiol. Cell Physiol.* 284:C738–C748. http://dx.doi.org/10.1152/ajpcell.00389.2002

Kosinski, C.M., C. Schlangen, F.N. Gellerich, Z. Gizatullina, M. Deschauer, J. Schiefer, A.B. Young, G.B. Landwehrmeyer, K.V. Toyka, B. Sellhaus, and K.S. Lindenberg. 2007. Myopathy as a first symptom of Huntington's disease in a Marathon runner. *Mov. Disord.* 22:1637–1640. http://dx.doi.org/10.1002/mds.21550

Ladd, A.N., N. Charlet, and T.A. Cooper. 2001. The CELF family of RNA binding proteins is implicated in cell-specific and developmentally regulated alternative splicing. *Mol. Cell. Biol.*

21:1285–1296. http://dx.doi.org/10.1128/MCB.21.4.1285-1296.2001

Lee, K.Y., M. Li, M. Manchanda, R. Batra, K. Charizanis, A. Mohan, S.A. Warren, C.M. Chamberlain, D. Finn, H. Hong, et al. 2013. Compound loss of muscleblind-like function in myotonic dystrophy. *EMBO Mol. Med.* 5:1887–1900. http://dx.doi.org/10.1002/emmm.201303275

Lin, L., J.W. Park, S. Ramachandran, Y. Zhang, Y.T. Tseng, S. Shen, H.J. Waldvogel, M.A. Curtis, R.L. Faull, J.C. Troncoso, et al. 2016. Transcriptome sequencing reveals aberrant alternative splicing in Huntington's disease. *Hum. Mol. Genet.*:ddw187. http://dx.doi.org/10.1093/hmg/ddw187

Lin, X., J.W. Miller, A. Mankodi, R.N. Kanadia, Y. Yuan, R.T. Moxley, M.S. Swanson, and C.A. Thornton. 2006. Failure of MBNL1-dependent post-natal splicing transitions in myotonic dystrophy. *Hum. Mol. Genet.* 15:2087–2097. http://dx.doi.org/10.1093/hmg/ddl132

Livak, K.J., and T.D. Schmittgen. 2001. Analysis of relative gene expression data using real-time quantitative PCR and the $2^{-\Delta\Delta C(T)}$ method. *Methods.* 25:402–408. http://dx.doi.org/10.1006/meth.2001.1262

Lodi, R., A.H. Schapira, D. Manners, P. Styles, N.W. Wood, D.J. Taylor, and T.T. Warner. 2000. Abnormal in vivo skeletal muscle energy metabolism in Huntington's disease and dentatorubropallidoluysian atrophy. *Ann. Neurol.* 48:72–76. http://dx.doi.org/10.1002/1531-8249(200007)48:1<72::AID-ANA11>3.0.CO;2-I

Lueck, J.D., A.E. Rossi, C.A. Thornton, K.P. Campbell, and R.T. Dirksen. 2010. Sarcolemmal-restricted localization of functional ClC-1 channels in mouse skeletal muscle. *J. Gen. Physiol.* 136:597–613. http://dx.doi.org/10.1085/jgp.201010526

Luthi-Carter, R., S.A. Hanson, A.D. Strand, D.A. Bergstrom, W. Chun, N.L. Peters, A.M. Woods, E.Y. Chan, C. Kooperberg, D. Krainc, et al. 2002. Dysregulation of gene expression in the R6/2 model of polyglutamine disease: parallel changes in muscle and brain. *Hum. Mol. Genet.* 11:1911–1926. http://dx.doi.org/10.1093/hmg/11.17.1911

MacDonald, M.E., C.M. Ambrose, M.P. Duyao, R.H. Myers, C. Lin, L. Srinidhi, G. Barnes, S.A. Taylor, M. James, N. Groot, et al. The Huntington's Disease Collaborative Research Group. 1993. A novel gene containing a trinucleotide repeat that is expanded and unstable on Huntington's disease chromosomes. *Cell.* 72:971–983. http://dx.doi.org/10.1016/0092-8674(93)90585-E

Mankodi, A., M.P. Takahashi, H. Jiang, C.L. Beck, W.J. Bowers, R.T. Moxley, S.C. Cannon, and C.A. Thornton. 2002. Expanded CUG repeats trigger aberrant splicing of ClC-1 chloride channel pre-mRNA and hyperexcitability of skeletal muscle in myotonic dystrophy. *Mol. Cell.* 10:35–44. http://dx.doi.org/10.1016/S1097-2765(02)00563-4

Mielcarek, M., M. Toczek, C.J. Smeets, S.A. Franklin, M.K. Bondulich, N. Jolinon, T. Muller, M. Ahmed, J.R. Dick, I. Piotrowska, et al. 2015. HDAC4-myogenin axis as an important marker of HD-related skeletal muscle atrophy. *PLoS Genet.* 11:e1005021. http://dx.doi.org/10.1371/journal.pgen.1005021

Mykowska, A., K. Sobczak, M. Wojciechowska, P. Kozlowski, and W.J. Krzyzosiak. 2011. CAG repeats mimic CUG repeats in the misregulation of alternative splicing. *Nucleic Acids Res.* 39:8938–8951. http://dx.doi.org/10.1093/nar/gkr608

Niccolini, F., S. Haider, T. Reis Marques, N. Muhlert, A.C. Tziortzi, G.E. Searle, S. Natesan, P. Piccini, S. Kapur, E.A. Rabiner, et al. 2015. Altered PDE10A expression detectable early before symptomatic onset in Huntington's disease. *Brain.* 138:3016–3029. http://dx.doi.org/10.1093/brain/awv214

Orvoen, S., P. Pla, A.M. Gardier, F. Saudou, and D.J. David. 2012. Huntington's disease knock-in male mice show specific anxiety-like behaviour and altered neuronal maturation. *Neurosci. Lett.* 507:127–132. http://dx.doi.org/10.1016/j.neulet.2011.11.063

Pette, D., and G. Vrbová. 1992. Adaptation of mammalian skeletal muscle fibers to chronic electrical stimulation. *Rev. Physiol. Biochem. Pharmacol.* 120:115–202.

Pierno, S., A. De Luca, C.L. Beck, A.L. George Jr., and D. Conte Camerino. 1999. Aging-associated down-regulation of ClC-1 expression in skeletal muscle: phenotypic-independent relation to the decrease of chloride conductance. *FEBS Lett.* 449:12–16. http://dx.doi.org/10.1016/S0014-5793(99)00202-1

Ponzio, T.A., C. Yue, and H. Gainer. 2007. An intron-based real-time PCR method for measuring vasopressin gene transcription. *J. Neurosci. Methods.* 164:149–154. http://dx.doi.org/10.1016/j.jneumeth.2007.04.012

Rattray, I., E. Smith, R. Gale, K. Matsumoto, G.P. Bates, and M. Modo. 2013. Correlations of behavioral deficits with brain pathology assessed through longitudinal MRI and histopathology in the R6/2 mouse model of HD. *PLoS One.* 8:e60012. http://dx.doi.org/10.1371/journal.pone.0060012

Ribchester, R.R., D. Thomson, N.I. Wood, T. Hinks, T.H. Gillingwater, T.M. Wishart, F.A. Court, and A.J. Morton. 2004. Progressive abnormalities in skeletal muscle and neuromuscular junctions of transgenic mice expressing the Huntington's disease mutation. *Eur. J. Neurosci.* 20:3092–3114. http://dx.doi.org/10.1111/j.1460-9568.2004.03783.x

Schiaffino, S., and C. Reggiani. 2011. Fiber types in mammalian skeletal muscles. *Physiol. Rev.* 91:1447–1531. http://dx.doi.org/10.1152/physrev.00031.2010

Sellier, C., F. Rau, Y. Liu, F. Tassone, R.K. Hukema, R. Gattoni, A. Schneider, S. Richard, R. Willemsen, D.J. Elliott, et al. 2010. Sam68 sequestration and partial loss of function are associated with splicing alterations in FXTAS patients. *EMBO J.* 29:1248–1261. http://dx.doi.org/10.1038/emboj.2010.21

She, P., Z. Zhang, D. Marchionini, W.C. Diaz, T.J. Jetton, S.R. Kimball, T.C. Vary, C.H. Lang, and C.J. Lynch. 2011. Molecular characterization of skeletal muscle atrophy in the R6/2 mouse model of Huntington's disease. *Am. J. Physiol. Endocrinol. Metab.* 301:E49–E61. http://dx.doi.org/10.1152/ajpendo.00630.2010

Standen, N.B., and P.R. Stanfield. 1980. Rubidium block and rubidium permeability of the inward rectifier of frog skeletal muscle fibres. *J. Physiol.* 304:415–435. http://dx.doi.org/10.1113/jphysiol.1980.sp013333

Steele, A.D., W.S. Jackson, O.D. King, and S. Lindquist. 2007. The power of automated high-resolution behavior analysis revealed by its application to mouse models of Huntington's and prion diseases. *Proc. Natl. Acad. Sci. USA.* 104:1983–1988. http://dx.doi.org/10.1073/pnas.0610779104

Strand, A.D., A.K. Aragaki, D. Shaw, T. Bird, J. Holton, C. Turner, S.J. Tapscott, S.J. Tabrizi, A.H. Schapira, C. Kooperberg, and J.M. Olson. 2005. Gene expression in Huntington's disease skeletal muscle: a potential biomarker. *Hum. Mol. Genet.* 14:1863–1876. http://dx.doi.org/10.1093/hmg/ddi192

Sun, X., P.P. Li, S. Zhu, R. Cohen, L.O. Marque, C.A. Ross, S.M. Pulst, H.Y.E. Chan, R.L. Margolis, and D.D. Rudnicki. 2015. Nuclear retention of full-length HTT RNA is mediated by splicing factors MBNL1 and U2AF65. *Sci. Rep.* 5:12521. http://dx.doi.org/10.1038/srep12521

Talmadge, R.J. 2000. Myosin heavy chain isoform expression following reduced neuromuscular activity: potential regulatory mechanisms. *Muscle Nerve.* 23:661–679. http://dx.doi.org/10.1002/(SICI)1097-4598(200005)23:5<661::AID-MUS3>3.0.CO;2-J

Talmadge, R.J., and R.R. Roy. 1993. Electrophoretic separation of rat skeletal muscle myosin heavy-chain isoforms. *J. Appl. Physiol.* 75:2337–2340.

Talmadge, R.J., W. Acosta, and T. Garland Jr. 2014. Myosin heavy chain isoform expression in adult and juvenile mini-muscle mice bred for high-voluntary wheel running. *Mech. Dev.* 134:16–30. http://dx.doi.org/10.1016/j.mod.2014.08.004

Turner, C., J.M. Cooper, and A.H. Schapira. 2007. Clinical correlates of mitochondrial function in Huntington's disease muscle. *Mov. Disord.* 22:1715–1721. http://dx.doi.org/10.1002/mds.21540

Urbanek, M.O., and W.J. Krzyzosiak. 2016. RNA FISH for detecting expanded repeats in human diseases. *Methods.* 98:115–123. http://dx.doi.org/10.1016/j.ymeth.2015.11.017

Wang, D., L. Zhong, M.A. Nahid, and G. Gao. 2014. The potential of adeno-associated viral vectors for gene delivery to muscle tissue. *Expert Opin. Drug Deliv.* 11:345–364. http://dx.doi.org/10.1517/17425247.2014.871258

Waters, C.W., G. Varuzhanyan, R.J. Talmadge, and A.A. Voss. 2013. Huntington disease skeletal muscle is hyperexcitable owing to chloride and potassium channel dysfunction. *Proc. Natl. Acad. Sci. USA.* 110:9160–9165. http://dx.doi.org/10.1073/pnas.1220068110